

1 Fault seal modelling – the influence of fluid
2 properties on fault sealing capacity in hydrocarbon
3 and CO₂ systems

4 **This is non peer-reviewed original version of the manuscript that has been**
5 **submitted for publication in Petroleum Geoscience. The final published**
6 **version is available via the 'Peer-reviewed Publication DOI' link on the right-5**
7 **hand side of the webpage.**

8 Rūta Karolytė^{1*}, Gareth Johnson^{1,a}, Graham Yielding² and Stuart M.V. Gilfillan³

9 ¹ Department of Earth Sciences, University of Oxford, 3 S Parks Rd, Oxford OX1
10 3AN

11 ²Badley Geoscience Ltd, North Beck House/North Beck Lane, Spilsby PE23 5NB

12 ^apresent address: Department of Civil and Environmental Engineering, University of
13 Strathclyde, James Weir Building, 75 Montrose St, Glasgow G1 1XJ

14 *Author for correspondence: ruta.karolyte@earth.ox.ac.uk

15 Keywords: fault seal; hydrocarbons; CO₂; interfacial tension; wettability; contact
16 angle; fluid properties; Otway Basin.

17 Abstract

18 Fault seal analysis is a key part of understanding the hydrocarbon trapping
19 mechanisms in the petroleum industry. Fault seal research has also been expanded
20 to CO₂-brine systems for the application to Carbon Capture and Storage (CCS). The
21 wetting properties of rock-forming minerals in the presence of hydrocarbons or CO₂
22 are a source of uncertainty in the calculations of capillary threshold pressure, which
23 defines the fault sealing capacity. Here we explore this uncertainty in a comparison
24 study between two fault-sealed fields located in the Otway Basin, south-east
25 Australia. The Katnook field in the Penola Trough is a methane field, while Boggy
26 Creek in Port Campbell contains a high-CO₂/methane mixture. Two industry
27 standard fault seal modelling methods (Yielding et al., 2010; Sperrevik et al., 2002)

28 are used to discuss their relative strengths and applicability to the CO₂ storage
29 context. We identify a range of interfacial tensions and contact angle values in the
30 hydrocarbon-water system under the conditions assumed by the Yielding et al.
31 (2010) method. Based on this, the uncertainty related to the spread in fluid
32 properties was determined to be 24% of the calculated threshold capillary pressure
33 value. We propose a methodology of threshold capillary pressure conversion from
34 hydrocarbon-brine to the CO₂-brine system, using an input of appropriate interfacial
35 tension and contact angle under reservoir conditions. The method can be used for
36 any fluid system where fluid properties are defined by these two parameters.

37 1 Introduction

38 Faults can be either pathways for, or barriers to fluid migration in the
39 subsurface and to the surface. Fault seal analytical techniques have been
40 developed to improve the prediction of hydrocarbon traps suitable for exploration.
41 More recently, fault seal research has expanded to applications to Carbon Capture
42 and Storage (CCS), where faults can act to: decrease the maximum storage
43 capacity of the reservoir; become unwanted barriers to fluid migration along the
44 planned injection pathway, causing pressure increase and limiting the maximum rate
45 of injection; or, provide a conduit for leakage of CO₂.

46 Two distinct methodologies of predictive modelling of the threshold capillary
47 pressure, which is a proxy for fault sealing capacity to hydrocarbons, have been
48 developed in the last two decades: one based on a calibration of a global dataset of
49 known sealing faults (Bretan et al., 2003; Yielding et al., 2010), and another, based
50 on laboratory measurements of fault samples (Sperrevik et al., 2002). Both of these
51 techniques have been widely applied to hydrocarbon systems. Fault capacity to seal
52 for CO₂ has been explored in theoretical studies (Iglauer, 2018; Miocic et al., 2019;
53 Naylor et al., 2010), yet there have been few attempts to test the methodology with
54 real geological examples (Bretan, 2016; Bretan et al., 2011; Yielding et al., 2011).

55 In terms of practically applying model results to either exploration of
56 hydrocarbons or CO₂ sequestration, the subject of interest is not the exact threshold
57 capillary pressure of a certain fault but rather the implications of that value to the
58 desired industrial activity. In exploration, this is applied to estimate maximum column
59 height and determine the economic viability of production. It is therefore important to

60 estimate how the uncertainty associated with the predictive method impacts the
61 prospect. In the context of CO₂ storage, threshold capillary pressure is used to
62 define the reservoir storage capacity. In this case the aim is not to overpressure the
63 fault and thus cause leakage. The practical use of fault seal modelling therefore
64 requires a good understanding of the uncertainty associated with the two different
65 approaches.

66 The interfacial tension (IFT) and the contact angle (CA) are the main fluid-
67 specific properties controlling the capillary seal and the key parameters used in both
68 hydrocarbon and CO₂ studies. The wetting properties of various rock-forming
69 minerals are different for CO₂ and hydrocarbons, which has caused a concern that
70 the seal rocks proven to retain hydrocarbon columns might be less sealing to CO₂
71 (Chiquet et al., 2007b; Daniel and Kaldi, 2009; Guariguata-Rojas and Underhill,
72 2017; Tenthorey et al., 2014). A recent study by Miocic et al. (2019) explored the
73 interplay between uncertainties in CA, IFT and fault rock composition in the CO₂-
74 brine system. The results highlighted that higher phyllosilicate content in the fault
75 rock reduces the threshold capillary pressure in the CO₂-brine system due to the
76 wettability of the clay minerals in the presence of CO₂, especially at depths > 1 km.

77 Our understanding of CA and IFT primarily relies on empirical measurements,
78 meaning that significant uncertainty exists in both hydrocarbon and CO₂-brine
79 systems. While the above concerns are valid for the CO₂ storage, the existing
80 uncertainties associated with CA and IFT also exist in the hydrocarbons. This is
81 because of the wide range of chemical compositions of crude oil and the difficulty of
82 sampling undegassed reservoir fluids.

83 In this contribution we investigate the uncertainty associated with the fluid
84 properties (CA, IFT) as well as geological assumptions required for the model (depth
85 at the time of faulting and maximum burial depth) in two field examples. One,
86 methane gas field in South Australia (Katnook), and another, a high CO₂/methane
87 mixture in Port Campbell, Victoria (Boggy Creek). In both cases, a gas column is
88 supported by the fault rock and the column height is known. The fields are located in
89 the Otway Basin, which is very well characterised in respect to hydrocarbon
90 exploration as well as CO₂ storage. These case studies therefore provide a realistic
91 example of the level of uncertainties that can be expected in future potential CO₂
92 storage sites.

93 This approach allows us to verify if the model predictions are valid and
94 systematically compare the uncertainties in the CO₂ and methane system. Fault seal
95 analysis is performed using the Sperrevik et al. (2002) and Yielding et al. (2010)
96 fault seal modelling methods, discussing the differences in the modelling
97 approaches, their associated uncertainties and suitability for the CO₂-brine system.
98 The former method inherently allows the conversion from mercury-air system to
99 CO₂-brine, while the latter method is calibrated to a hydrocarbon system. We
100 summarise the current understanding of the IFT and CA ranges in hydrocarbons
101 that the Yielding et al. (2010) method is based on to define the expected IFT and CA
102 distribution and their mean values. Based on this, we propose a new calibration of
103 the Yielding et al. (2010) algorithm to the CO₂-brine system.

104 2 Fault rock seal dependencies

105 Fault rock seals occur when movement along a fault plane creates a low-
106 permeability fault rock, and depend on the fault rock composition as well as the
107 properties of the fluids in the system. In siliciclastic sand-shale sequences, the
108 sealing fault rocks are characterised by continuous clay-rich smears (Lindsay et al.,
109 1993). Their thickness is favoured by greater thickness of shale beds in host rocks,
110 weight of the overburden, and burial depth (Lehner and Pilaar, 1997). Quartz
111 cementation at temperatures above 90 °C or ~>3 km further decreases fault rock
112 porosity and increases the sealing potential (Fisher and Knipe, 1998; Rimstidt and
113 Barnes, 1980). The resulting fault rock may act as baffle to fluid migration through a
114 process of capillary sealing, which is created by the opposing forces between the
115 two phases at their interface – the wetting phase (water or brine) and the non-
116 wetting phase (hydrocarbons or CO₂, in this context) (Fisher and Knipe, 1998; Watts,
117 1987; Yielding et al., 1997). Capillary seals fail when the fluid buoyancy pressure
118 exceeds the threshold capillary pressure. Capillary threshold pressure (P_c) is
119 therefore a key fault rock attribute used in the hydrocarbon exploration industry to
120 determine the sealing potential of the fault and calculate maximum column heights
121 (h_{max}), using the relationship between the height of the fluid column and the
122 buoyancy pressure it exerts on the sealing rocks (Schowalter, 1974):

$$123 \quad P_c = \frac{2IFT \times \cos\theta}{r} \quad (1)$$

124
$$h_{max} = \frac{P_c}{(\rho_h - \rho_w)g} \quad (2)$$

125 Where IFT is the interfacial tension between the fluids, θ is the contact angle,
126 r is the effective pore throat radius, ρ is density, g is acceleration due to gravity, h
127 and w denote hydrocarbons and water.

128 The interfacial tension and contact angle (or wettability) are the key
129 properties controlling capillary seal and depend on many factors including pressure,
130 temperature, fluid type, fluid density and rock mineralogy (e.g. Iglaier et al., 2015;
131 Nordgard Bolas et al., 2005; Øren and Bakke, 2003; Radke et al., 1992; Schowalter,
132 1974). The influence of these factors is a key concern in describing fault zone
133 behaviour. The advantage, however, is that the characteristics of fluids and their
134 affinity to reservoir rock can be approximated by these two input parameters, and
135 therefore applied in the same manner to systems involving hydrocarbons, CO₂ or
136 any other fluid type of interest.

137 The buoyancy pressure exerted on the fault rock by the column of fluid is
138 greater with increasing density contrast between the wetting and the non-wetting
139 phases. Under typical reservoir conditions, density of methane ranges between 100
140 – 300 kg/m³, CO₂ is approximately 400 – 600 kg/m³ and oil density varies between
141 700 – 1000 kg/m³ (Danesh, 1998). Brine density depends on salinity and has a
142 value of 1000-1150 kg/m³. It is therefore apparent, that a fault rock with a certain
143 capillary threshold pressure would retain a smaller column of methane than of CO₂
144 or oil, if the other parameters were the same. However, the differences in interfacial
145 tension and CA between CO₂ and hydrocarbons also impact the threshold capillary
146 pressure of the fault rock in a CO₂-brine system (Chiquet et al., 2007b). The
147 interplay between IFT, CA and fluid density therefore is key to consider in applying
148 fault seal modelling techniques to CO₂ sequestration.

149 The effective pore throat radius of a fault zone is impossible to directly
150 determine, and by standard practice is approximated using a predictive algorithm
151 based on the clay content of the faulted rocks, such as SGR (Yielding et al., 1997).
152 Two different approaches have been developed to link SGR to capillary threshold
153 pressure. One approach is based on laboratory experiments of mercury-air injection
154 tests in micro-fault samples and subsequent correlation of measured capillary

155 pressures to sample clay content (Sperrevik et al., 2002), based on earlier studies
156 by Knipe (1997), Gibson (1998). The second approach uses data from known
157 hydrocarbon traps sealed by faults to empirically correlate the maximum observed
158 buoyancy pressures (assumed equivalent to threshold pressure) to SGR values
159 (Bretan et al., 2003; Yielding, 2002; Yielding et al., 2010). The two approaches have
160 been termed 'deterministic' and 'empirical' respectively (Yielding et al., 2010), and
161 will be referred to as such in the forthcoming text. The two methods are often used
162 in conjunction and have been shown to produce similar results in certain but not all
163 SGR/burial depth configurations (Yielding et al., 2010). To date, the application of
164 these methods to the CO₂-brine systems has been limited (Bretan et al., 2011).

165 The deterministic approach is based on laboratory measurements of fault
166 rock permeability from a variety of fault structures within reservoir core samples and
167 requires a conversion from the mercury-air system to hydrocarbon-water or CO₂-
168 brine system by using appropriate values for IFT and contact angle between the
169 fluid and the wetting phase (Sperrevik et al., 2002). In contrast, the empirical
170 approach (Bretan et al., 2003; Yielding, 2002) is based on a calibration of SGR
171 values and across-fault buoyancy pressure differences of known sealing faults.
172 Importantly, the calibration includes only hydrocarbons at depths greater than 1.5
173 km. This means that theoretically, the method can only be applied to fluid systems
174 which fall within the range of IFT and contact angle parameters as the hydrocarbon
175 field used in the calibration. Further constraining this range is discussed below
176 before we propose a methodology to convert fault seal modelling results from
177 hydrocarbons to CO₂-brine system.

179 3 Geological background

180 In this study we describe two gas fields in the Otway Basin, Victoria, Australia: The
181 Katnook field in the Penola Trough and the Boggy Creek field in the Port Campbell
182 embayment. Below we outline the geology of the fields in terms of stratigraphy, trap
183 geometries and gas charge.

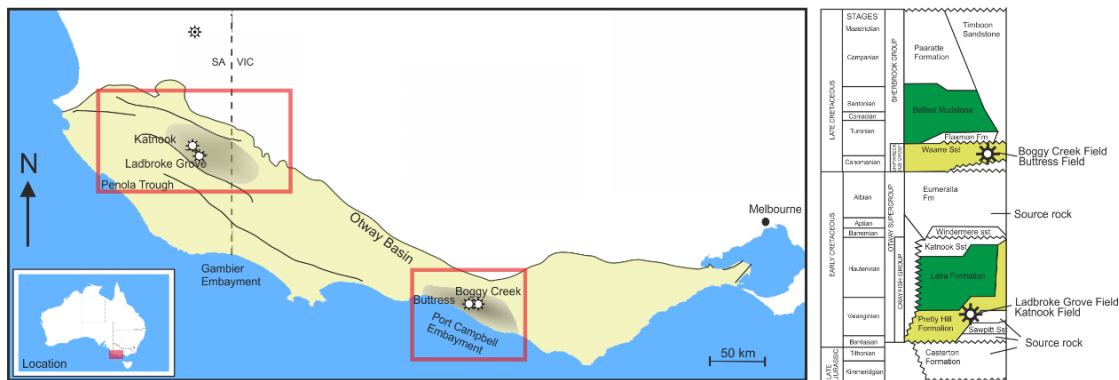
184 3.1 Basin stratigraphy

185 The present day geometry of the Otway Basin was developed during the
186 Cretaceous to Miocene rifting with a period of inversion in the mid-Cretaceous, when
187 the rift axis moved south (Teasdale et al., 2003). A series of graben and half-graben
188 structures consist of compartmentalised fault-bound reservoirs, with numerous
189 hydrocarbon and CO₂ accumulations (Fig. 1). Two case studies discussed here
190 present examples of gas column retention by a fault rock in a situation of reservoir-
191 reservoir juxtaposition. Katnook in the Penola Trough is a methane field, while the
192 Boggy Creek field in Port Campbell contains a high-CO₂/methane mixture.

193 The two fields are within different reservoir formations at different
194 stratigraphic intervals (Fig. 1). The Katnook field is stratigraphically lower, located in
195 Pretty Hill Formation of 2 - 4.5 km thickness, within the Pretty Hill Sandstone. The
196 main target reservoir is the Pretty Hill Sandstone member at the top of the sequence
197 (Lyon et al., 2005). The formation consists of massive, slumped and cross-bedded
198 sand packages, classified as lith-arenites to feldspathic lith-arenites (Little and
199 Phillips, 1995). The Laira Formation forms a regional seal, comprised of siltstones
200 and shales interbedded with sandstones. The Katnook sandstone at the top of the
201 Crayfish Group (consisting of both the reservoir and the seal lithologies) is also gas-
202 bearing, but is not a subject to this discussion. Katnook-1 and 2 are production wells
203 targeting Katnook sandstone within the Crayfish Group, while Katnook-3 produces
204 from the deeper Pretty Hill Formation. Shale units within the lower parts of the Pretty
205 Hill Formation and the underlying Casterton Formation are the oil and gas source
206 rocks in the Penola Trough and the SW part of the basin (Boreham et al., 2004).

207 The Boggy Creek CO₂ field is stratigraphically higher, within the Waarre
 208 Sandstone, comprised of interbedded siltstones and shales, segregated into four
 209 units defined by depositional environments. Unit C, the main reservoir interval, is
 210 poorly sorted, medium to coarse-grained quartz arenite (Watson et al., 2004). The
 211 underlying Eumeralla Formation consist of inter-bedded lithic sandstones, siltstones,
 212 coals and claystones (Cockshell et al., 1995). The deeper coal-rich units of
 213 Eumeralla Formation are the source rocks in the SE part of the basin. The Belfast
 214 Mudstone overlies the reservoir and forms a regional seal (Boreham et al., 2004).

215 The Waarre sandstone is approx. 90 m thick and the main producing interval
 216 within it (Unit C) is 25 -40 m thick (Dance, 2013). The underlying Eumeralla
 217 Formation is up to 3 km thick (Cockshell et al., 1995). Significant oil shows have
 218 been observed within the Eumeralla Formation in other parts of the basin (Lisk,
 219 2004) and therefore good connectivity between the Waarre and Eumeralla units is
 220 expected despite the silt and clay inter-beds.

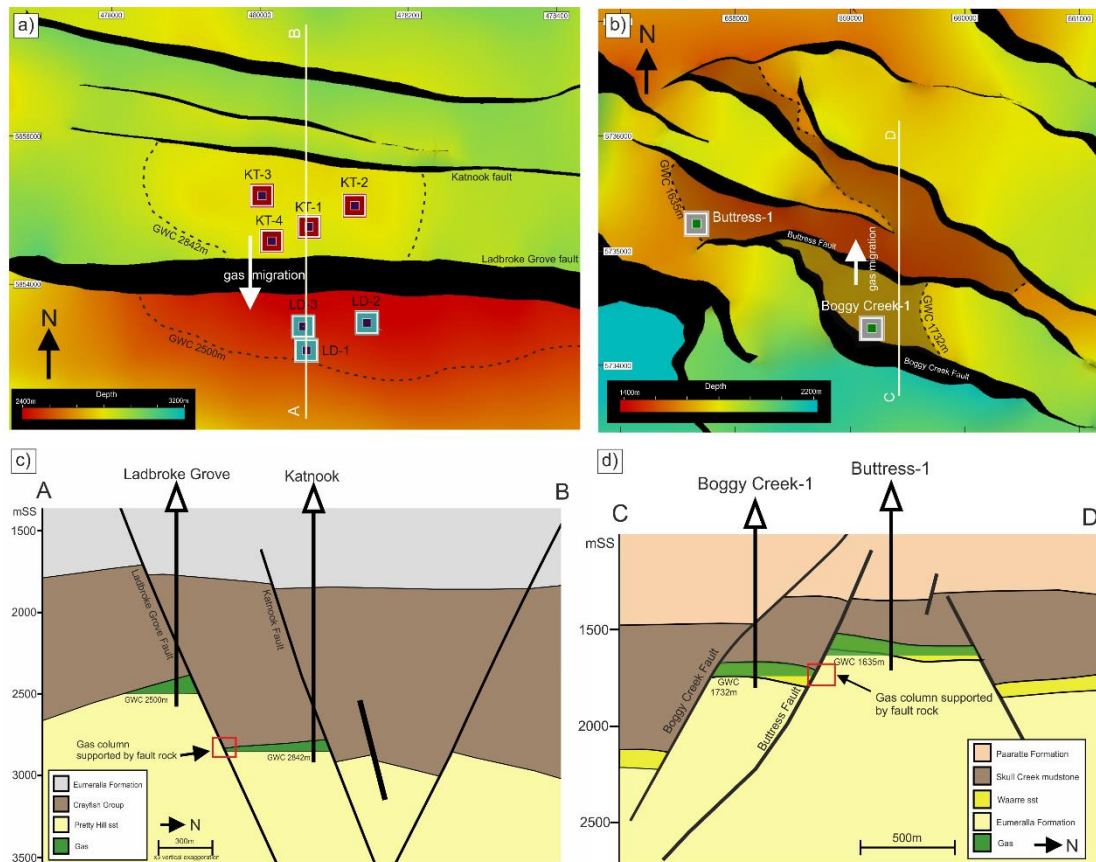


221
 222 *Figure 1. Location map of Penola Trough (Katnook/Ladbroke Grove fields) and Port*
 223 *Campbell (Buttress/Boggy Creek fields). Both localities are within the Otway Basin. Inset on*
 224 *the right shows the location of both reservoirs within the stratigraphic column (adapted from*
 225 *Lyon et al., 2004).*
 226

227 3.2 Trap geometry

228 The Katnook field is bound by the Katnook fault to the north and Ladbroke
 229 Grove fault to the south (Fig. 2a). The northern side of the field is juxtaposition-
 230 sealed against Crayfish Group shales, while the southern side reaches the Ladbroke
 231 Grove Fault, where the reservoir is self-juxtaposed (Fig. 2c). The Boggy Creek field
 232 is bound by the Boggy Creek Fault to the south and the Buttress Fault to the north

233 (Fig. 2b). Similarly to the Katnook field, the main seal to the reservoir is provided by
 234 juxtaposition seal to the south, but fault rock seal exists to the north (Fig. 2d).



235
 236 *Figure 2. Map and cross-sectional views of Penola Trough (a, c) and Port Campbell (c, d)*
 237 *gas field locations. a) Map view of the top of the Pretty Hill reservoir horizon, coloured by*
 238 *depth. b) Map view of the top of the Waarre sandstone reservoir horizon, coloured by depth.*
 239 *c) Cross-section view of line A-B from figure (a). Ladbroke Grove and Katnook fields in*
 240 *Penola Trough. Cross-section drawn from seismic data using 3x vertical exaggeration.*
 241 *Katnook field is supported by Katnook fault to the north (juxtaposition seal) and Ladbroke*
 242 *Grove fault to the south (fault rock seal). d) C-D cross-section view (from figure b) of the*
 243 *Boggy Creek and Buttress fields in Port Campbell. Cross-section drawn from seismic data*
 244 *without vertical exaggeration. Boggy Creek gas field is retained by juxtaposition seal to the*
 245 *south and fault rock seal to the north. The adjacent Buttress field is structurally higher.*
 246
 247

248 3.3 The sequence of gas charge events

249 The two main phases of hydrocarbon generation in the Otway Basin are
 250 estimated at mid-Cretaceous (Boult et al., 2004) and mid-Paleogene (Duddy, 1997),
 251 based on thermal maturation modelling and the relationship between GWC positions
 252 above spill points and known gas diffusion rates (Lyon et al., 2005). Early oil/wet gas
 253 charge was flushed or diluted by later dry gas charge (Boreham et al., 2004).

254 Methane charge was followed by a later stage magmatic CO₂ injection (Chivas et al.,
255 1987; Lyon et al., 2005; Watson et al., 2003). Due to the sealing or partially sealing
256 nature of bounding faults, the CO₂/methane ratio significantly varies across
257 geographically closely located fields.

258 The Ladbroke Grove field contains CO₂, with higher concentrations at the
259 base (49%) and lower at the top of the reservoir interval (27%). The Katnook field
260 contains primarily methane with only trace amounts of CO₂ (0.2%). ³He/⁴He,
261 CO₂/³He and neon isotopic ratios indicate that CO₂ in Ladbroke Grove is of mantle
262 origin (³He/⁴He = 1.46 R/R_A) (Karolytè, 2018). ³He/⁴He ratios in the Katnook field are
263 slightly elevated above the crustal values (0.06 R/R_A), but any mantle-sourced noble
264 gases are decoupled from the migrating CO₂ (Karolytè, 2018). These geochemistry
265 results suggest that methane has likely migrated through the fault rock from Katnook
266 to the Ladbroke Grove field, while the later CO₂ charge was restricted to Ladbroke
267 Grove only.

268 The Boggy Creek and Buttress fields both contain mixtures of mantle CO₂
269 and methane. CO₂ concentrations within the traps increase with depth because of
270 its higher density, and Boggy Creek (87% CO₂) is more CO₂-rich than Buttress (77%
271 CO₂) (Karolytè et al., 2019). While independent charge to both fields cannot be
272 completely excluded, the observed concentration gradient suggests that CO₂ was
273 first charged to the Boggy Creek field, and later migrated to Buttress. The trap is not
274 filled up to the spill point, suggesting this migration occurred through the fault rock
275 which supports the column.

276

277 4 Methods

278 4.1 Geological 3D models

279 This work has been undertaken using a compilation of existing industry and
280 academic datasets. 3D model development, structural and fault seal analysis was
281 undertaken using TrapTester™ software. The Penola Trough 3D model was
282 developed by Paul Lyon and published in Lyon et al. (2005b, 2007, 2004). It was
283 constructed by interpretation of the 3D Balnaves-Haselgrove seismic survey in time

284 and pseudo-depth (Lyon et al., 2004). The 3D model used for Port Campbell area
285 was developed by Ziesch et al. (2017) using a combination of OGF93A, ONH01 and
286 Curdie Vale 3D seismic surveys. Seismic data reinterpretation in this study has led
287 to addition of some new faults and modification of fault and horizon geometries in
288 the original models.

289 4.1.1 V-shale

290 The V-shale curves for the studied wells were created from GR wireline logs.
291 'Clean sand' and 'pure shale' (0 and 100% V-shale) values were determined by
292 correlating GR measurements to core descriptions and, where possible, core
293 permeability tests from the well completion reports. The Waarre sandstone is
294 feldspathic (Watson et al., 2003), which is reflected in the relatively high chosen API
295 (American Petroleum Institute unit) values of clean sands. The strength of the GR
296 signal is often not uniform between different wells, in which case different clean
297 sand and pure shale values have to be chosen to produce internally consistent V-
298 shale logs. The V-shale values were calculated using the linear response equation
299 (Asquith et al., 2004):

$$300 \quad V_{Shale} = I_{GR} = \frac{GR_{log} - GR_{sand}}{GR_{shale} - GR_{sand}} \quad (3)$$

301

302 **4.1.2 Fault seal modelling**

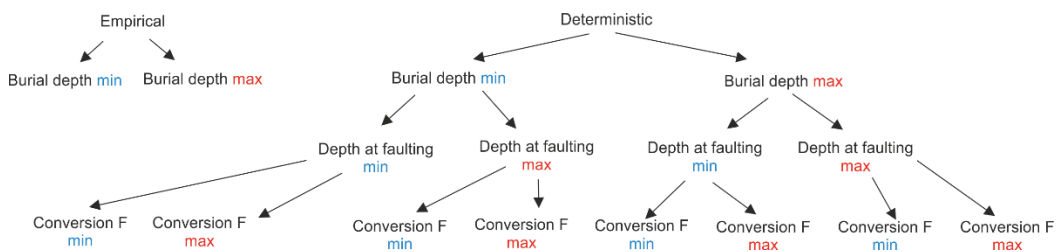
303 The intersection lines between the top of the reservoir formation on the
304 footwall and the hanging wall side of the fault were created on the fault planes (e.g.
305 Yielding & Freeman, 2016). Manual quality check techniques such as projecting
306 seismic slices on the fault plane were used to accurately map out the geometry of
307 the intersections. Allan diagrams (Allan, 1989) were created to identify the areas of
308 interest where reservoir formation is juxtaposed against another permeable rock on
309 the other side of the fault.

310 Buoyancy pressure is calculated on the 3D surface of the fault based on the
311 input of gas and water pressure gradient and the gas water contact (GWC). This
312 data was obtained from repeat formation tester (RFT) plots in well completion
313 reports (WCRs) from Buttress and Ladbroke Grove fields. Pressure profile data did
314 not exist for Katnook and Boggy Creek fields, so gas pressure gradients were
315 calculated from gas densities. Gas densities at reservoir conditions were calculated
316 using the Peng-Robinson equation of state (Peng and Robinson, 1976). A summary
317 of input parameters relevant to buoyancy pressure calculation is given in Table 1.

319 **Table 1. Summary of parameters used in the buoyancy pressure calculations. Temperature and**
 320 **pressure relevant where density was calculated using equation of state rather than obtained**
 321 **from RFT measurements. Major gas compositions are from Karolyt  (2018) and Karolyt  et al.**
 322 **(2019).**

Field	Temperature �C	Pressure MPa	GWC mSS	P_w kg/m ³	P_g kg/m ³	Major gas composition		
						C ₁₊	N ₂	CO ₂
Penola Trough								
Ladbroke Grove	104	23	2500	927	244	45	7.2	325 49
Katnook	118	28	2842	1035	125	97	3.2	326
Port Campbell								
Buttress	62	16	1635	1035	382	22	1.9	327 77
Boggy Creek	59	17	1732	1035	456	10	2.0	328 87
								329

330 d on the 3D plane of the fault using the input of V-shale curves. The threshold
 331 capillary pressures were calculated using two different SGR calibration techniques:
 332 empirical and deterministic. Both of these methods require an input of the maximum
 333 burial depth. The empirical method uses the burial depth to categorize faults for
 334 three different seal envelopes (< 3 km, 3 - 3.5 km, 3.5 – 5 km), while the
 335 deterministic method directly incorporates the value. The deterministic method
 336 additionally requires an estimate of the depth at the time of faulting and a conversion
 337 factor from mercury-air to gas-brine system, which is dependent on the interfacial
 338 tension between the wetting and non-wetting phases and the wettability of the
 339 system. A minimum and maximum estimate of each of the parameters were
 340 determined based on known reservoir conditions and a literature review, resulting in
 341 two and eight possible scenarios for the empirical and deterministic methods,
 342 respectively (Fig. 3). Both of these methods ascribe threshold capillary pressures to
 343 every point of the 3D fault surface. These can then be compared to the known
 344 buoyancy pressure exerted by the gas column trapped in the reservoir.



345 **Figure 3. Schematic diagram of different scenarios including minimum and maximum**
 346 **estimates of parameters required by the empirical and deterministic methods.**
 347

348

349 4.1.3 Input parameters

350 The input parameters used in the fault seal modelling are summarised in
351 Table 2, and the reasoning is explained below.

352 **Table 2. Summary of parameters used in fault seal modelling**

Field	Burial depth (m) (for deterministic)		Burial depth (m) (for empirical)		Depth at the time of faulting (m)		Conversion factor	
	min	max	min	max	min	max	min	max
Boggy Creek	1623	1783	<3000	-	450	1200	0.054	0.087
Katnook	2787	2987	<3000	3000- 3500	800	1200	0.111	0.133

353

354

355 4.1.3.1 Maximum burial depth

356 The Otway Basin has undergone two significant phases of uplift and
357 denudation, but the effects are less significant at the margins of the basin where the
358 two case studies are situated. A comprehensive basin-wide sonic transit time study
359 by (Tassone et al., 2014) suggests that Port Campbell is close to its maximum burial
360 depth, with a net exhumation range obtained from Boggy Creek-1 indicating 0 – 160
361 m net exhumation. The same is true for Penola Trough, where conservative
362 estimate of net exhumation is in the range of 0 - 200 m. This is confirmed by vitrinite
363 reflectance and apatite fission track data (Boult and Hibburt, 2002; Duddy, 1997).
364 The upper end of this range gives a maximum burial depth of 2987 m, which is very
365 close to the cut-off value of 3 km between different seal envelopes in Yielding et al.
366 (2010) method. We therefore consider two scenarios of < 3 km and 3 - 3.5 km
367 maximum burial depth for the Penola Trough.

368 4.1.3.2 Depth at the time of faulting

369 4.1.3.2.1 Penola Trough

370 The main faulting event was contemporaneous with the Early Cretaceous
371 rifting which coincided with the deposition of the regional seal formation. The
372 sediments of the Crayfish Group commonly drape over major structural highs,
373 indicating that faulting had ceased by the end of its deposition (Briguglio et al., 2015)
374 and was inactive during the deposition of the overlying Eumeralla Formation (Boult

375 et al., 2008), which is also evident from the seismic data. The depth of Ladbrooke
376 Grove fault at the time of displacement is therefore constrained by the total
377 thickness of the Crayfish Group. The current thickness of the Crayfish Group in the
378 Katnook well is 800 m, which is also the thickest in the Penola Graben. Structural
379 cross-section balance and restoration indicates that 400 m of Crayfish sediments
380 were removed in the Penola Graben (Briguglio et al., 2015). Depth at the time of
381 faulting is therefore constrained to 800 - 1200 m.

382 **4.1.3.2.2 Port Campbell**

383 The seal formation, consisting of a succession of mudstones overlain by
384 Skull Creek mudstone, varies in thickness across the faults, indicating syn-
385 sedimentary faulting (Ziesch et al., 2015). The faulting ceased during the deposition
386 of the unconformably overlain Wangerrip Group in Paleocene. Depth at the time of
387 faulting is therefore represented by the thickness of this group, which ranges from
388 450 to 1200 m.

389 **4.1.4 Conversion factor**

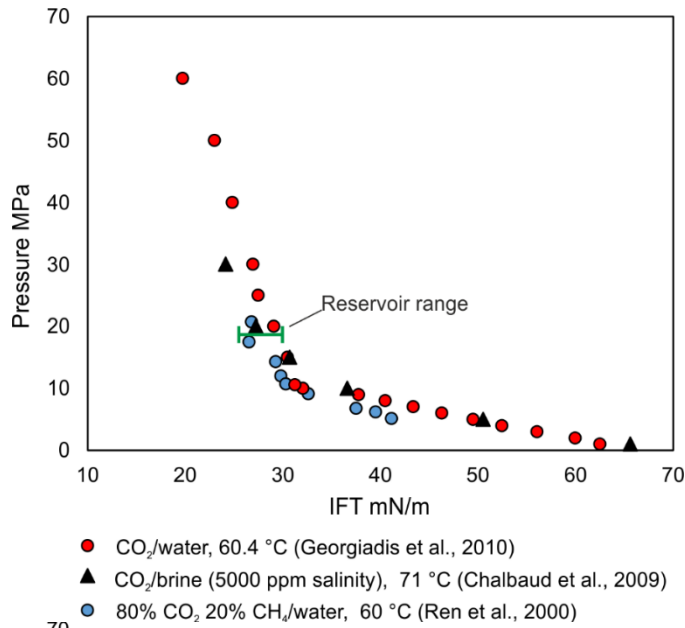
390 The conversion factor from mercury-air to the chosen wetting and non-
391 wetting phase requires an input of IFT and contact angle:

$$392 \quad P_{wn} = P_{ma} \times \frac{IFT_{wn} \times \cos\theta_{wn}}{IFT_{ma} \times \cos\theta_{ma}} \quad (4)$$

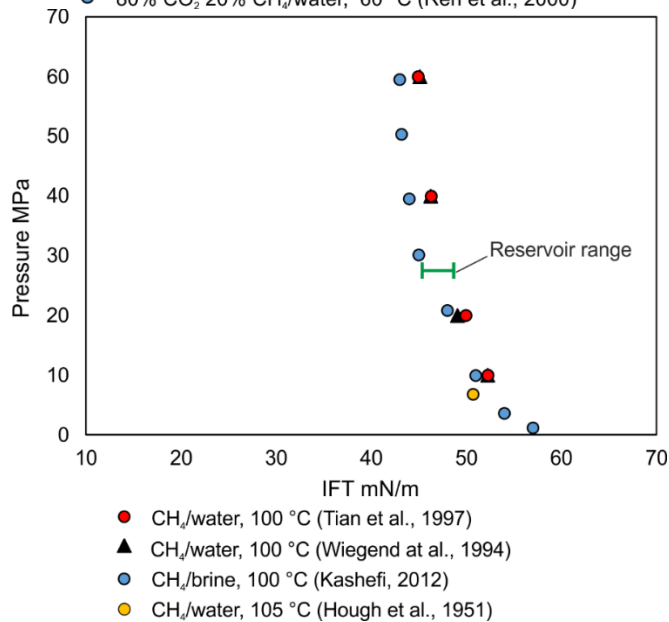
393 where P is threshold capillary pressure, θ is the contact angle, wn and ma denote
394 wetting/non-wetting phase of choice and mercury/air, respectively.

395 IFT has a strong dependency on pressure and temperature for both CO_2
396 and methane, so assessment for local reservoir conditions is imperative. Figure 4
397 shows a compilation of results selected from laboratory studies under conditions
398 similar to those in Boggy Creek and Katnook reservoirs. Presented data include
399 CH_4 -water, CO_2 -water, CO_2 -brine and CO_2 - CH_4 mixtures in water (Chalbaud et al.,
400 2009; Georgiadis et al., 2010; Hough et al., 1951; Kashefi, 2012; Ren et al., 2000;
401 Wiegand and Franck, 1994; Yi-Ling et al., 1997). The range constrained for the
402 Boggy Creek field is 26 - 32 mN/m (Fig. 4). Admixture of CH_4 to pure CO_2 generally
403 increases the IFT, but as shown in Figure 4a, the measurements in mixtures

404 containing < 20% methane are not significantly different from CO₂-water system
 405 (Ren et al., 2000). The IFT range expected in Katnook methane field is 47-49 mN/m
 406 (Fig. 4b).



407



408

409

410

411

412

Fig. 4. IFT vs pressure for a) Boggy Creek reservoir conditions b) Katnook reservoir conditions. Green line shows the expected range for reservoir pressure.

413

414

415

416

Typical reservoir rocks are often considered to be water-wet in the presence of hydrocarbons (e.g. Schowalter, 1974; Vavra et al., 1992), with some exceptions, including grain coating with high polarity of crude oil components (Singh et al., 2016). The Penola Trough traps show evidence for early charge of oil which was later displaced by gas (Higgs et al., 2015; Lovibond et al., 1995), therefore a range of 0-

417 30° contact angles is taken to reflect the potential effect of acid adsorption on grain
418 surfaces.

419 The wettability of CO₂-brine-mineral system has been investigated by a
420 growing number of studies (Bikkina, 2011; Farokhpour et al., 2013; Jung and Wan,
421 2012), most commonly directly on single mineral surfaces, where minerals are
422 required to be ultraclean and smooth on an atomic level for reproducible results. The
423 results are highly variable (0 - 90°), but much of the variation is attributed to the
424 surface roughness and sample preparation practices (Iglauer et al., 2015). However,
425 the most consistent findings include a contact angle increase by up to 30° at CO₂
426 transition from the gaseous to the supercritical phase (Jung and Wan, 2012;
427 Sutjiadi-Sia et al., 2008). In the absence of minerals known to be particularly
428 hydrophobic in the presence of CO₂ in the reservoir, the expected contact angle
429 range for Boggy Creek is taken to be 10 - 40°, as expected for common silicate and
430 carbonate reservoir minerals (Espinoza and Santamarina, 2010).

431 Given the defined range of IFT and contact angles for both reservoirs,
432 minimum and maximum conversion factors calculated for Boggy Creek Field (CO₂-
433 dominated) and Katnook Field (methane-dominated) were 0.054 - 0.087 and 0.111 -
434 0.133, respectively.

435

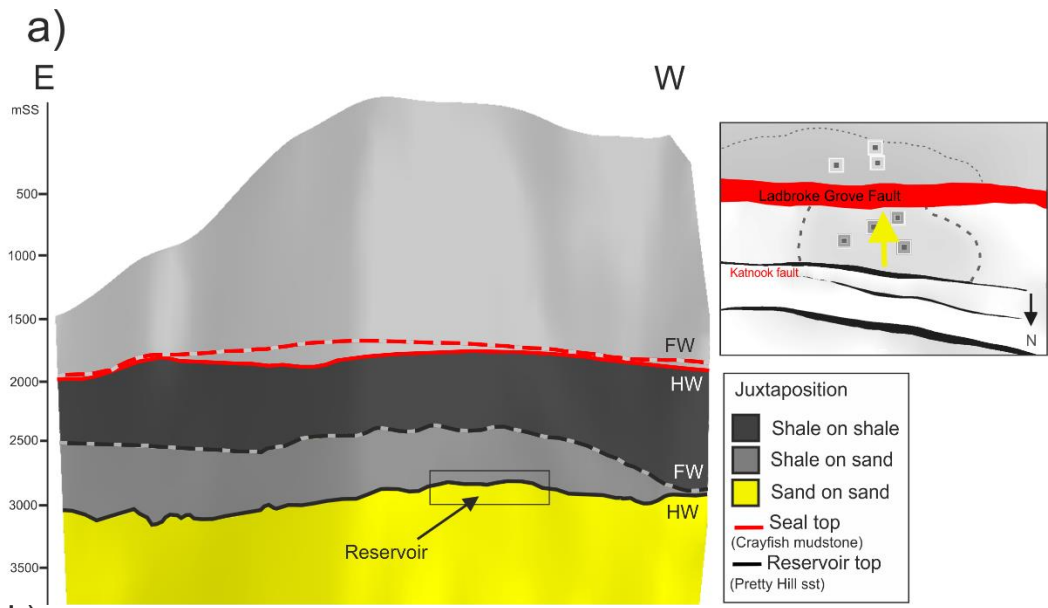
436

437 5 Results

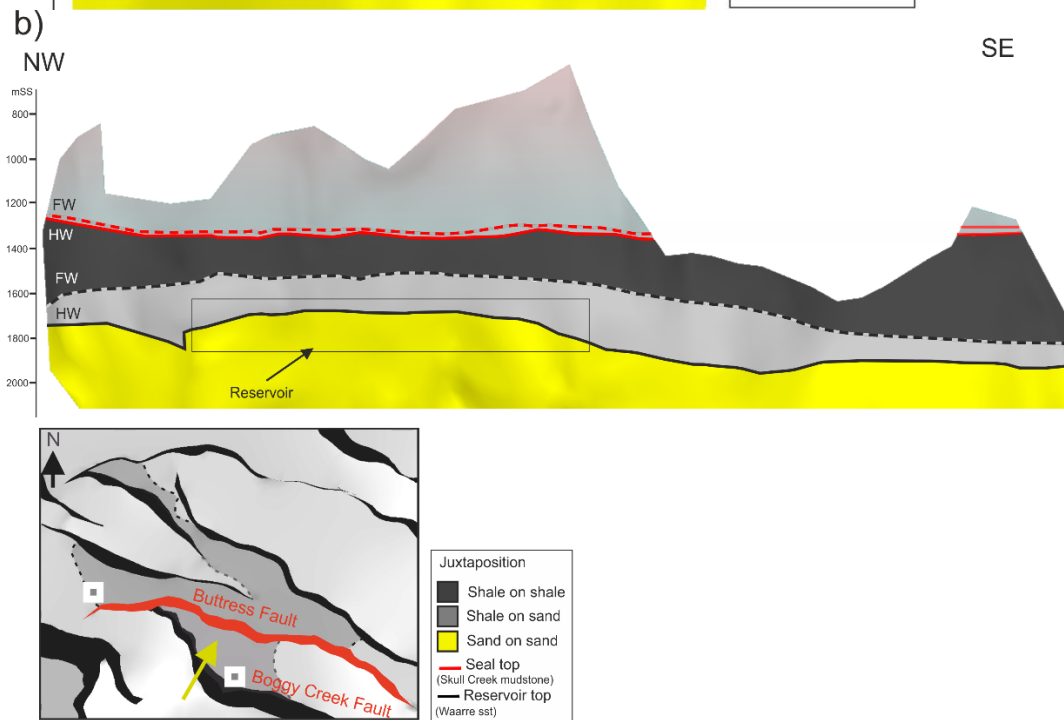
438 5.1 Juxtaposition

439 The Allan diagrams in Figure 5 show the juxtaposition of lithologies along the
440 strike of the fault planes for Katnook (a) and Boggy Creek (b) reservoirs. The
441 Katnook reservoir is primarily sealed by sand on shale juxtaposition by the Katnook
442 fault to the north, but the field extends to the hanging wall of the Ladbroke Grove
443 fault which is supporting the column to the south (Fig. 7.5a). The entire extent of the
444 reservoir is juxtaposed against reservoir on the other side of the fault. Similarly, the
445 Boggy Creek field is supported by sand on shale juxtaposition in the footwall of the
446 Boggy Creek fault to the south. The field extends to the hanging wall of the Buttress
447 fault (Fig. 5b), where the reservoir is self-juxtaposed for the entire extent of the gas
448 field. Calculated V-shale values for areas of reservoir self-juxtaposition range
449 between 20 and 50% on the Ladbroke Grove Fault and 10% to 80% on the Buttress
450 fault. SGR values above 20% are considered to be sealing (Yielding et al., 2010), so
451 in both cases the model indicates that the faults are acting as barriers to gas
452 migration.

453



454



455

456

457

458

459

460

461

462

463

Figure 5. Allan diagrams showing juxtaposition along the strike-view of the faults, viewed from the hanging wall side. Insets show the location of the faults (marked in red), the yellow arrows show the direction of view. a) Ladbrooke Grove fault, supporting the southern side of the Katnook gas field (3x vertical exaggeration). b) Buttress fault, supporting the northern side of the Boggy Creek gas field (no vertical exaggeration). Black rectangles show the extent of the gas-bearing reservoir. Horizon intersections on the fault plane are displayed as dashed lines for the footwall side and solid lines for the hanging wall side.

464

465 5.2 Threshold capillary pressure

466 Across fault leakage through capillary seal breach commonly occurs near the
467 top of the trap structure, where buoyancy pressure is the highest. The critical (and
468 therefore most likely to leak) points occur where the lowest SGR values coincide
469 with the highest buoyancy pressure on a given fault plane. The buoyancy pressure
470 values identified at these points are 0.28 MPa for the Katnook field and 0.29 MPa for
471 the Boggy Creek.

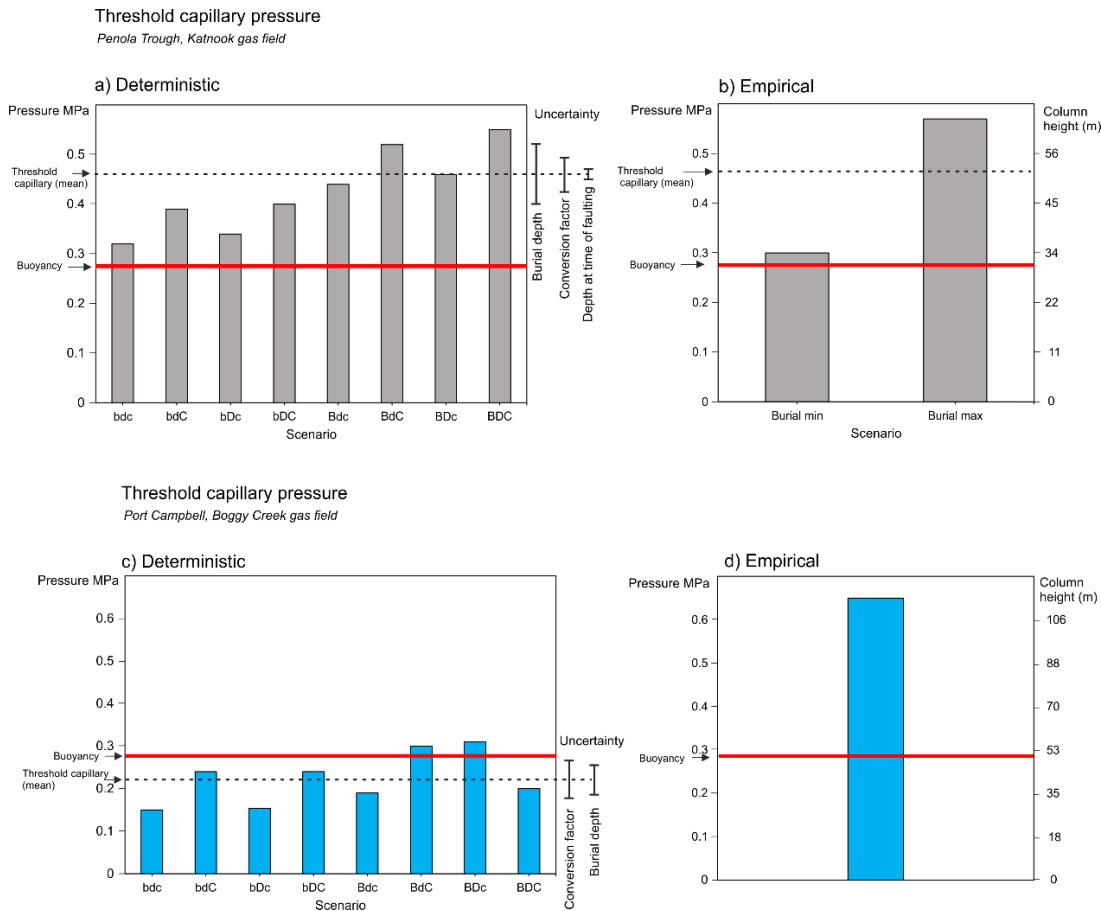
472 The calculated threshold capillary and buoyancy pressures can then be
473 compared at the critical points, where the difference between them represents the
474 amount of extra pressure (or extra gas column) the fault can retain before seal
475 breach. Figure 6 shows the results of the deterministic (a, c) and empirical (b, d)
476 calibrations for Katnook and Boggy Creek fields.

477 The results from both calibrations for the Katnook methane gas field indicate
478 that the current live gas column of 31 metres (equivalent to 0.28 MPa buoyancy
479 pressure) is stable but the fault is close to being critically pressured. The threshold
480 capillary pressures range from 0.32 to 0.55 MPa, equivalent to a total column of gas
481 between 35 to 57 m according to the deterministic calibration. Empirical calibration
482 suggests the fault seal will be breached at pressures between 0.3 and 0.57 MPa,
483 equivalent to a total gas column of 33 to 63 m. The results from both calibrations are
484 remarkably similar, with the average threshold capillary pressure of 0.42 and 0.43
485 MPa using the deterministic and empirical methods respectively.

486 The deterministic and empirical methods provide different results for the
487 Boggy Creek CO₂ field. The fault is currently supporting a 51 m column of gas,
488 equivalent to a buoyancy pressure of 0.29 MPa. This is close to the upper range
489 values predicted by the deterministic method. The threshold capillary pressure
490 ranges from 0.15 to 0.31 MPa (26 – 55 m of total column height). The predicted
491 average column height is 39 m, slightly under-predicting the sealing potential of the
492 fault. In contrast, the empirical calibration indicates a threshold pressure of 0.65
493 MPa and a maximum column height of 115 m, which is more than double the current
494 amount.

495 The empirical method requires only one parameter of the maximum burial
496 depth. The deterministic method requires three parameters. In the case of the
497 Katnook methane field, the uncertainty in maximum burial depth has the biggest
498 impact on the results and the conversion factor is the second largest uncertainty
499 (see y axis annotation on Fig. 6). In contrast, the uncertainty in the conversion factor
500 has a greater impact on the Boggy Creek CO₂ field results than the maximum burial
501 depth.

502 The structural spill point at the Katnook field is identified at 2891 m, which
503 effectively allows a maximum gas column height of 81 m. In Boggy Creek, the
504 structural spill point occurs at 1956 m, allowing a maximum column height of 272 m.
505 The maximum column heights identified from the structural perspective of the traps
506 are all higher than those modelled by fault seal analysis. This means that filling the
507 traps to the maximum fault-rock threshold pressures derived from all models would
508 not result in fill-to-spill and therefore both methods indicate that migration to the
509 adjacent fault trap occurred through the fault rather than through over-spilling.



511
 512 *Figure 6. Bar chart showing threshold capillary pressure results for the Katnook methane*
 513 *field (a, b) and the Bogy Creek CO₂ field (c, d) using deterministic (a, c) and empirical (b, d)*
 514 *SGR calibration algorithms. Conversion to column height displayed on the secondary y axis*
 515 *(same values applicable to both deterministic and empirical method graphs. Red line shows*
 516 *current column height/buoyancy pressure. The Katnook gas column is predicted to be stable*
 517 *by both methods with maximum threshold capillary pressure ranging from 0.32 to 0.55 MPa*
 518 *(deterministic) and 0.3 to 0.57 MPa (empirical). The Bogy Creek field is predicted to be*
 519 *within the upper end of the critical pressure zone by the deterministic method (0.15-0.31*
 520 *MPa) and stable by the empirical method. Labels in deterministic scenarios: B- maximum*
 521 *burial depth, D – depth at the time of faulting, C – conversion factor. Upper and lower case*
 522 *letter indicate maximum and minimum values respectively.*

523

524 6 Discussion

525 6.1 Addressing the uncertainty in fault seal modelling

526 The deterministic and empirical methods present a key difference in their
527 definition of the threshold capillary pressure. The deterministic method defines a
528 best fit line through the data points of measured capillary entry pressures during
529 injection experiments to fault rock samples. Therefore, by definition, the method
530 predicts the average threshold pressure for the modelled conditions. In contrast, the
531 fault seal envelopes defining the threshold capillary pressure in the empirical
532 method represent the upper limit of data for buoyancy pressures retained by fault
533 rocks with a given SGR. The threshold pressure returned by the empirical equation
534 is therefore a maximum estimate. In other words, even though the same term of
535 threshold capillary pressure is used by the two methods, the derived value
536 represents somewhat different concepts and presents a different level of uncertainty.

537 Some uncertainties are inherent to the modelling method and cannot be
538 easily accounted for. The deterministic method is based on threshold capillary
539 pressure measurements of micro-fault samples on the scale of millimetres to
540 centimetres (Sperrevik et al., 2002). The measured clay content of the fault
541 structures is assumed to be represented by SGR when upscaled to use in a
542 predictive way. The method is therefore applied on the assumption that kilometre
543 scale faults behave in the same way as micro structures. In reality this is not strictly
544 the case, with seismic-scale fault zones comprising clay smears, cataclastic zones
545 and multiple planes of deformation (Bense et al., 2016; Faulkner et al., 2010; Fisher
546 and Knipe, 1998; Pei et al., 2015; Shipton and Cowie, 2001), which all add to the
547 total sealing capacity of the fault zone. Detailed fault zone analyses show that the
548 permeability over individual fault zone components can vary considerably (e.g. over
549 3 orders of magnitude) (Shipton et al., 2002) and therefore upscaling one of those
550 components to be representative of the entire fault zone involves a significant
551 simplification.

552 The advantage of the empirical method in this respect is that SGR is
553 assumed to be a proxy for the fault sealing properties, which include shale content

554 but also various heterogeneous components of the fault zone. SGR calculated on
555 the 3D surface of the fault planes is the direct input in the calibration as well as in
556 the predictive workflow, which eliminates the uncertainty associated with equating
557 SGR to specific rock properties such as the true volume of shale. The compilation
558 dataset includes data from 7 different basins, covering a wider range of diagenetic
559 conditions relative to the deterministic method which is based on samples from the
560 North Sea (Yielding, 2002).

561 Some of the uncertainties associated with the local geological conditions and
562 fluid properties are parameterised in the deterministic method and therefore can be
563 accounted for. The error bars in Figure 6 a) and c) show the relative uncertainties
564 associated with the different model input parameters. For the two case studies
565 presented here, fluid properties (governing the conversion factor) present a higher
566 uncertainty for CO₂ rather than methane. This is primarily due to the larger IFT
567 range selected for CO₂, but does not suggest that the interfacial tension of CO₂ is
568 less characterised than that of methane. The larger range is due to a relatively
569 higher number of currently available studies, including measurements using different
570 salinity, salt types and gas mixtures, while methane laboratory studies are largely
571 constrained to pure methane and deionized water. In cases where fluid properties
572 are well defined, maximum burial depth is the most significant source of uncertainty,
573 while depth at the time of faulting is the least significant input parameter.

574 6.2 Uncertainty related to fluid properties

575 An important difference between the two methods is the approach to
576 accounting for the fluid properties. The interfacial tension and wettability are
577 parameterised in the deterministic method, making it more versatile, arguably
578 adaptive to CO₂-brine system and more precise in cases where fluid properties are
579 well characterised. The empirical method does not explicitly address the fluid
580 properties, but operates under the assumption that the range of IFT and contact
581 angle configurations in hydrocarbons is small, and that the possible variability of
582 fluid properties is represented in the global dataset compilation. The two important
583 issues with the empirical approach are:

584 a) the uncertainty related to fluid properties is undefined when applied to
585 hydrocarbons.

586 b) the application to CO₂ can only be considered valid in cases where CO₂
587 exhibits properties within the range of those observed in hydrocarbons.

588 These are explained in detail below.

589 6.3 a) Uncertainty related to fluid properties of 590 hydrocarbons in the empirical model

591 To further assess the empirical method application to CO₂, the uncertainty
592 related to the fluid properties of hydrocarbons has to be defined. The percentage
593 error of the capillary threshold pressure (δP_c) from the uncertainty in fluid properties
594 (as standard deviation) can therefore be expressed as, using Equation 1:

$$595 \quad \delta P_c = \frac{\sigma(P_c)}{\partial(P_c)} \times 100\% = \frac{\sigma(2IFT \times \cos\theta)}{\partial(2IFT \times \cos\theta)} \times 100\% \quad (5)$$

596 The empirical method uses a data compilation including both oil and
597 methane in reservoirs > 1.5 km depth (Yielding, 2002), and can be assumed to
598 reflect the general IFT and contact angle variability of all hydrocarbons at that depth.
599 The percentage error can therefore be calculated using a random sampling
600 modelling approach with inputs of the probability distribution of IFT and contact
601 angle values in hydrocarbons-brine system. Interfacial tension and contact angle are
602 assumed to be independent variables; even though some co-variation may exist,
603 currently it is not well understood and there are far more factors affecting the contact
604 angle not directly related to the fluid type.

605 6.3.1 Defining IFT and wettability range for hydrocarbons

606 The IFT between hydrocarbons and water (or brine) is primarily controlled by
607 the chemical composition of the hydrocarbons, the density contrast between the two
608 phases and temperature (Flock et al., 1986; Hassan et al., 1953; Rajayi and
609 Kantzas, 2011). Pressure mainly affects gas solubility in oil and therefore has a
610 bigger effect on oils with high dissolved gas content (Ghorbani and Mohammadi,
611 2017). Generally, the IFT in hydrocarbons is not well characterised and usually an
612 average IFT of 30-35 mN/m is used for capillary seal modelling purposes (Berg,
613 1975; Robert M. Sneider and Neasham, 1997). Considerable effort has been made

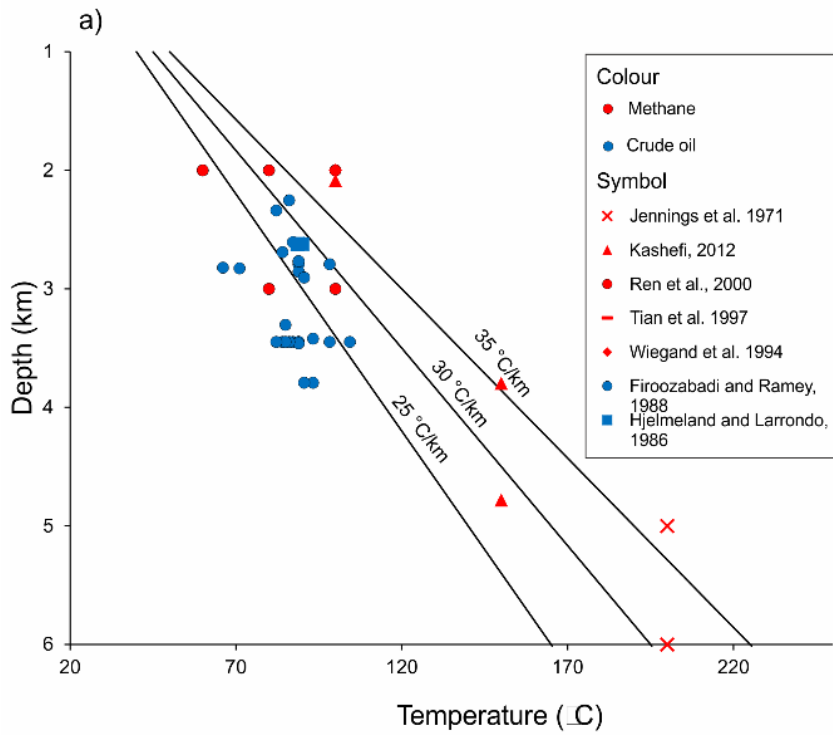
614 to characterise IFT of individual hydrocarbon compounds and derive predictive
615 equations to determine the IFT based on the input of reservoir temperature
616 (Kalantari Meybodi et al., 2016), density difference (Danesh, 1998; Sutton, 2006)
617 and critical fluid temperature (Najafi-Marghmaleki et al., 2016). However, these
618 methods are developed for data compilations of pure aromatics and alkanes, and do
619 not reflect the fluid properties of crude oil at reservoir conditions, which include high
620 percentage of other compounds such as naphthenes and asphaltics (Buckley et al.,
621 1997).

622 There have been relatively few studies presenting IFT measurements in
623 crude oil-water systems, but these can be considered the most reservoir-
624 representative. Figure 8 shows a compilation of laboratory measurements within the
625 envelope of pressures and temperatures valid for geothermal gradients between 25
626 and 35 °C/km and hydrostatic pressure gradient of 10 MPa/km. The compilation
627 includes samples of crude oil above bubble point representing non-degassed oils,
628 below-bubble point oils and methane. The IFT values of crude oil range 26-42 mN/m
629 and are more strongly controlled by chemical differences rather than depth. IFT of
630 methane decreases with depth and ranges from 40 to 53 mN/m. Based on this
631 example dataset, it is assumed that the IFT values of hydrocarbons used in the
632 empirical calibration method are expected to be within a uniform probability
633 distribution with a mean value of 39 ± 8 mN/m (Fig. 9a).

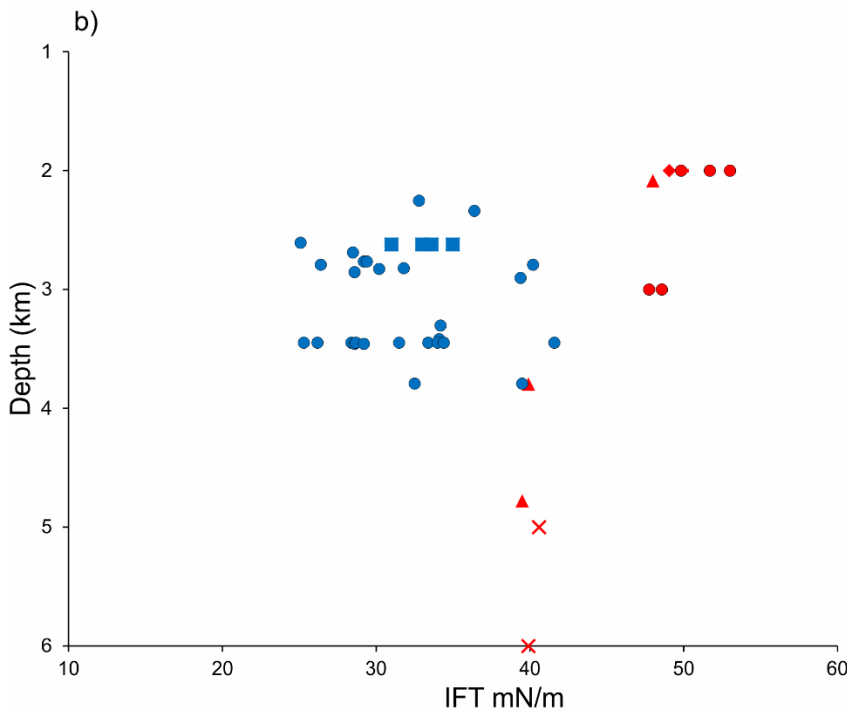
634 In the context of capillary seal modelling, reservoir formations are generally
635 considered to be water-wet in the presence of hydrocarbons (contact angle = 0°)
636 (e.g. Schowalter, 1974; Vavra et al., 1992). This is not strictly true, with mixed-wet
637 and oil-wet states often observed in hydrocarbon reservoirs (Treiber and Owens,
638 1972), often due to mineral surface coating with high polarity crude oil components
639 such as asphaltenes which have high affinity to the reservoir minerals (Alipour
640 Tabrizy et al., 2011; Singh et al., 2016). The degree of oil-wetting is expected to be
641 higher in reservoirs containing high maturity oil and in the presence of carbonate
642 cements, smectite, chlorite, kaolinite and iron-oxides (Barclay and Worden, 2009;
643 Worden and Morad, 2000). Because the contact angle directly affects the calculated
644 column heights and associated threshold capillary pressures, the practice of
645 assuming 0° contact angle in hydrocarbon reservoirs always provides a maximum
646 rather than conservative estimate. In the absence of strong statistical data, we
647 assume that reservoir rocks are more commonly water-wet than oil-wet in the

648 presence of hydrocarbons. This spread of data is best described by an exponential
649 probability distribution ($\beta = 15$), with a mean value of $15 \pm 15^\circ$ (Fig 9b) The lowest
650 values in the range are the most probable. Based on Equation 3, retention of a gas
651 column is only possible when the contact angle is $\leq 90^\circ$ ($\cos\theta > 0$). Because the
652 data set by definition only includes reservoirs with observed columns, contact angles
653 must range between 0 and 90° .

654



655



656

657

658

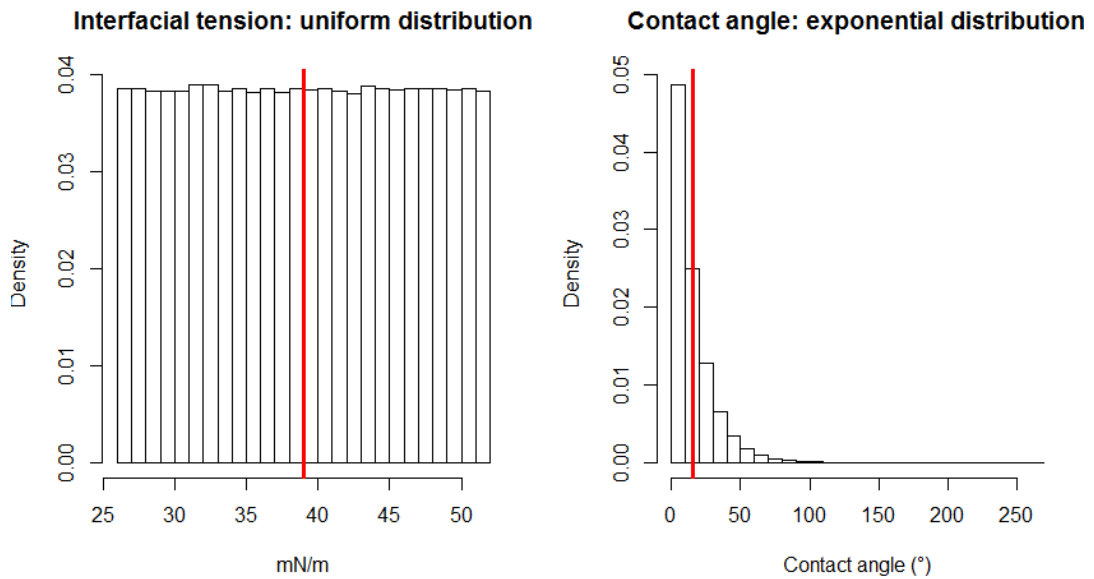
659

660

661

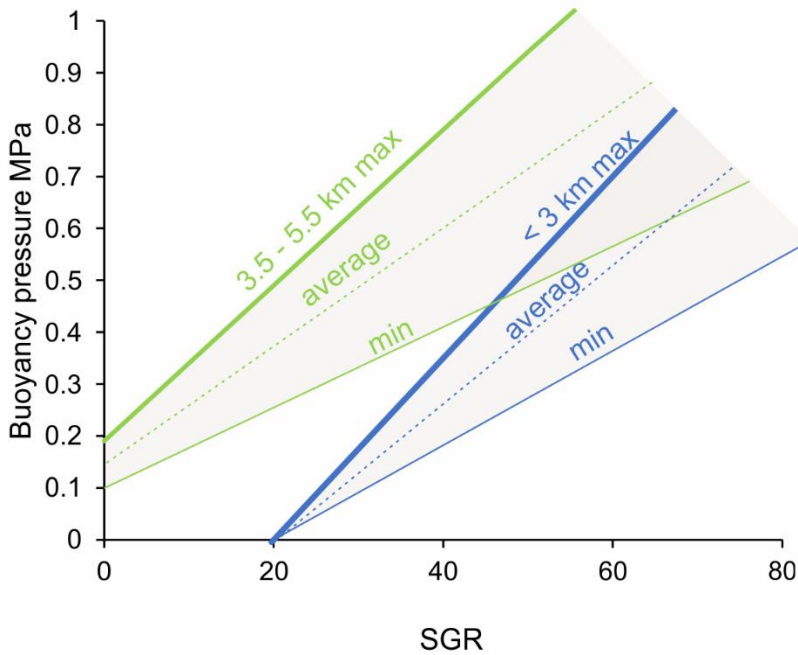
Figure 8. IFT of crude oil and methane data compilation from the literature, filtered to conditions applicable to geological pressure and temperature conditions (25 - 35 °C/km geothermal gradient). a) shows the distribution depth vs temperature conditions, b) shows the IFT values of the same data points. Crude oil IFT values range between 26 - 42 mN/m

662 and are uniformly distributed. Methane values range 40 - 53 mN/m and decrease with depth.
 663 Combined together, this data represents a uniform distribution.



664
 665 *Figure 9. Probability distribution of IFT (a) and contact angle (b) in hydrocarbons at reservoir*
 666 *conditions below 2 km depth, defined based on a literature review of laboratory studies*
 667 *(discussed in text). Red vertical line shows mean. IFT is expected to be uniformly distributed*
 668 *with a mean value of 39 ± 8 mN/m. Exponential distribution ($\beta = 15$) best describes the*
 669 *expected contact angle.*
 670

671 Based on the probability distributions of IFT and contact angle determined
 672 above, the percentage error of threshold capillary pressure (δP_c) determined from
 673 Equation 5 using Monte Carlo random sampling analysis ($n = 10^6$) is 24%. Figure 10
 674 shows the seal failure envelopes of the empirical model (Yielding et al., 2010) with
 675 the calculated error added. The seal envelopes define the upper boundary of all
 676 buoyancy pressures observed to be sealed by fault rocks and therefore statistically
 677 represent the higher values within the data distribution or maximum threshold
 678 capillary pressure. We can therefore use the calculated uncertainty to estimate the
 679 average threshold capillary pressure ($P_c - \sigma$) and minimum threshold capillary
 680 pressure ($P_c - 2\sigma$). The uncertainty increases with increasing P_c .



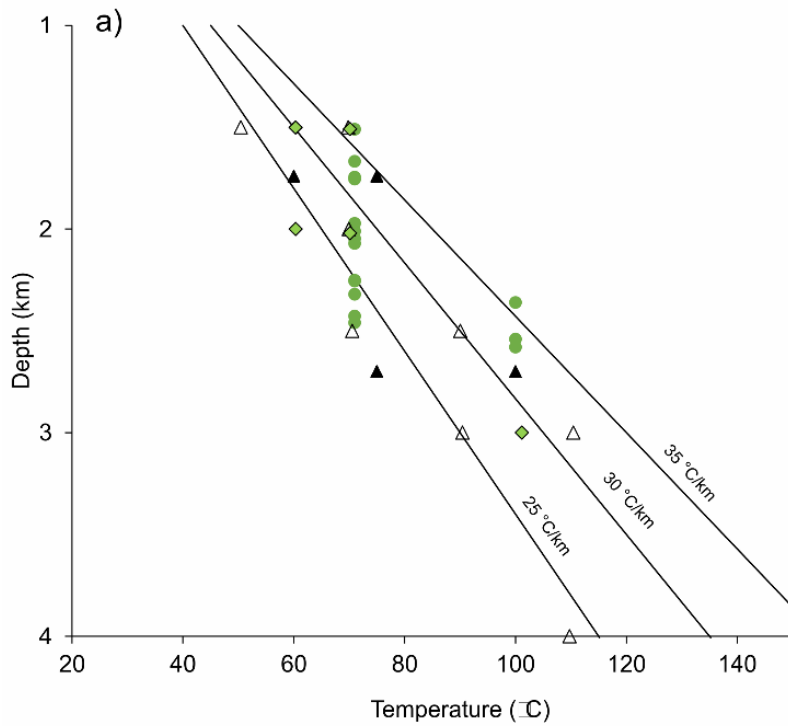
681
 682 *Figure 10. SGR vs Buoyancy pressure with < 3 km and 3.5 - 5.5 km threshold capillary*
 683 *pressure envelopes from Yielding et al. (2010). The thick solid line shows the original*
 684 *maximum threshold capillary pressure. Dashed lines show calculated average and minimum*
 685 *pressures for given burial depth brackets.*
 686

687 **6.3.1.1 Implications for use in hydrocarbons**

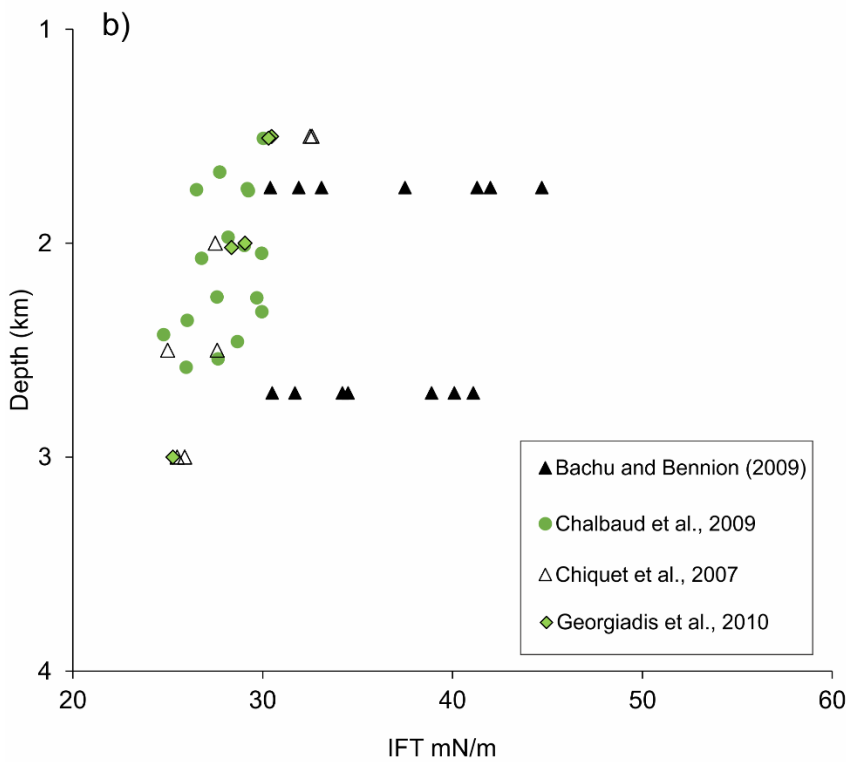
688 The calculated uncertainty envelopes do not change the interpretation of the
 689 empirical calibration method, but rather provide additional constraints that can be
 690 applied in variety of contexts. In cases where capillary pressure modelling is used to
 691 assess the economic viability of the reservoir, the uncertainty can be a useful input
 692 into the risking process. The average threshold capillary pressure value is better
 693 used in the calculation of likely hydrocarbon column heights, bearing in mind that the
 694 true column height can be controlled by many factors independent to fault seal such
 695 as structural spill points and charge. In cases where sufficient geological evidence
 696 exists to indicate that the trap has been filled, the calculated uncertainty envelope
 697 provides means to determine the minimum expected column. The average threshold
 698 capillary pressure value using the empirical method is also more comparable to the
 699 average results of the deterministic method (rather than using the current empirical
 700 max value) when the two are used in conjunction.

701 6.4 b) Empirical method applied to the fluid properties of
702 CO₂

703 In the last decade significant effort has gone into characterising IFT of CO₂
704 at a range of conditions, with existing data covering CO₂/water (Chiquet et al.,
705 2007a; Georgiadis et al., 2010) and CO₂/brine with variable salinity and salt types
706 (Bachu and Bennion, 2009; Chalbaud et al., 2009). IFT has been characterised for
707 mixtures of CO₂ and methane in water (Ren et al., 2000) and brine (Liu et al., 2016).
708 Increasing brine salinity has been shown to increase the IFT in CO₂/brine system
709 with significant deviations in saline and hypersaline conditions (Bachu and Bennion,
710 2009; Chalbaud et al., 2009; Liu et al., 2016). Figure 11 shows results from
711 published laboratory studies filtered to those representative of pressure and
712 temperature conditions in the subsurface (geothermal gradients 25 – 35 °C/km,
713 hydrostatic pressure gradient 10 MPa/km). The data includes pressures above 15
714 MPa (~1.5 km depth), which is in line with depths recommended for safe geological
715 CO₂ sequestration (> 1.2 km) (Miocic et al., 2016). It is apparent that in the
716 supercritical fluid state, depth does not significantly influence the IFT. The most
717 important controlling factor is brine salinity which increases the IFT due to increasing
718 density contrast between CO₂ and the brine. The maximum IFT values of 44.7 and
719 41.1 mN/m at 1.7 km and 2.7 km depth respectively from the study of Bachu and
720 Bennion (2009) are measured in brines of 334 g/L salinity, which is close to the
721 maximum possible salt saturation in water. In comparison, the salinity of UK oil and
722 gas fields ranges from 30 to 227 g/L with an average value of 130 g/L (Gluyas and
723 Hitchens, 2003). The IFT range presented here covers the minimum (CO₂-pure
724 water) to maximum (CO₂-hypersaline brine) geologically possible conditions relevant
725 to CO₂ sequestration context (> 1.5 km depth), and also falls within the range
726 observed in liquid hydrocarbons. The IFT values range between 26 to 45 mN/m,
727 which is remarkably similar to IFT range in crude oil (26 – 42 mN/m, Fig. 8).



728



729
730

731 *Figure 11. IFT of CO₂ in water and brine of different salinities, filtered to only display*
 732 *pressure and temperature conditions applicable to geological setting (25-35 °C/km*
 733 *geothermal gradient). a) shows the distribution depth vs temperature conditions, b) shows*
 734 *the IFT values of the same data points. IFT ranges 26-45 mN/m. Datapoints from Bachu and*
 735 *Bennion (2009) show the effects of increasing salinity, with a maximum of 334 g/L resulting*
 736 *in the highest IFT values.*

737 The wettability in CO₂-brine system is a complex issue and cannot be easily
738 defined as a bracket range for all reservoir conditions. The conditions of many
739 experimental set ups are very different to reservoir conditions, as discussed in
740 section 4.1.4, therefore the upscaling of single mineral experimental results to
741 reservoir is problematic Irrespective of this variation, the most significant observation
742 emerging from CO₂-brine lab studies is the change in wettability caused by pressure.
743 This is observed when CO₂ changes from gaseous to supercritical fluid phase at
744 around 8 MPa. It is presently not understood if the change in wettability is related to
745 the process of phase change or to the physical properties of supercritical CO₂.

746 In summary, the IFT values for CO₂ are similar to those of oil, while methane
747 IFT values are higher on average. The contact angles in CO₂-brine system present
748 a higher level of uncertainty and are hard to evaluate as a generic range. IFT and
749 contact angles can however be defined with higher confidence for specific reservoir
750 conditions, as exemplified by this study.

751 6.4.1 Conversion factor from hydrocarbons to CO₂

752 This work has defined an average value (μ) of the probability distributions of
753 IFT (39 mN/m) and CA (15°) for hydrocarbons under pressure and temperature
754 conditions included in the calibration dataset by Yielding et al. (2010). This means
755 that the calculated threshold capillary pressure of hydrocarbons can be converted to
756 CO₂-brine system for chosen IFT and CA values of CO₂:

$$757 \quad P_c(CO_2) = P_c \times \frac{IFT_{CO_2} \times \cos\theta_{CO_2}}{\mu IFT_h \times \mu \cos\theta_h} \quad (6)$$

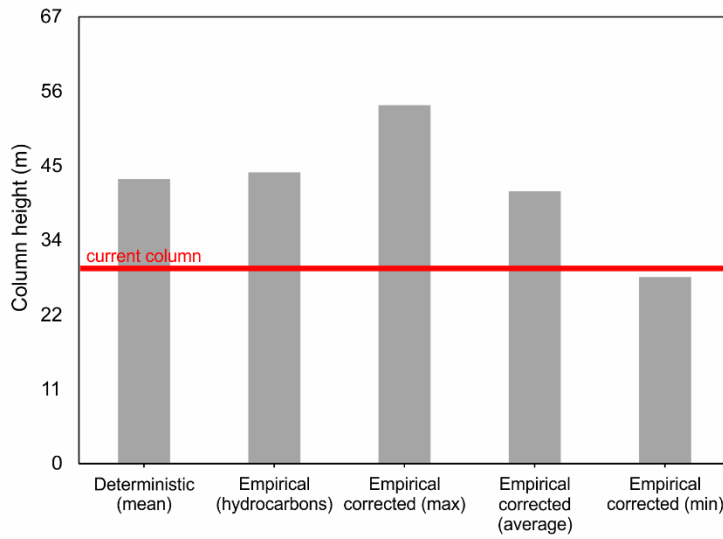
758 This can also be applicable to hydrocarbons in instances where IFT and CA
759 are well defined and significantly different to the average values.

760 Figure 12 shows calculated column heights calculated using the standard
761 empirical and deterministic methods, compared to the empirical model after
762 conversion to CO₂ using Equation 6 (maximum value) and calculated average and
763 minimum values. For the Katnook methane system, the correction factor increases
764 the column heights for methane due to higher IFT, but the overall change is not
765 significantly different from the original empirical model. The current column is
766 predicted to be stable regardless of the correction.

767 The maximum column height for the Boggy Creek CO₂ field is reduced by
768 the correction, with the average empirical value slightly higher than the column
769 height value known to be held by the fault. This prediction is in closer agreement to
770 the deterministic model, and is more likely to be correct based on the geochemistry
771 of the fields, indicating higher mantle CO₂ contents at Boggy Creek than in the
772 adjacent Buttress field and suggesting initial charge to Boggy Creek lead to
773 subsequent migration into Buttress. The current column in Boggy Creek is not near
774 the structural spill point, suggesting the CO₂ transfer between the fields occurred
775 through the fault rock, and the current column is therefore expected to be near the
776 threshold value.

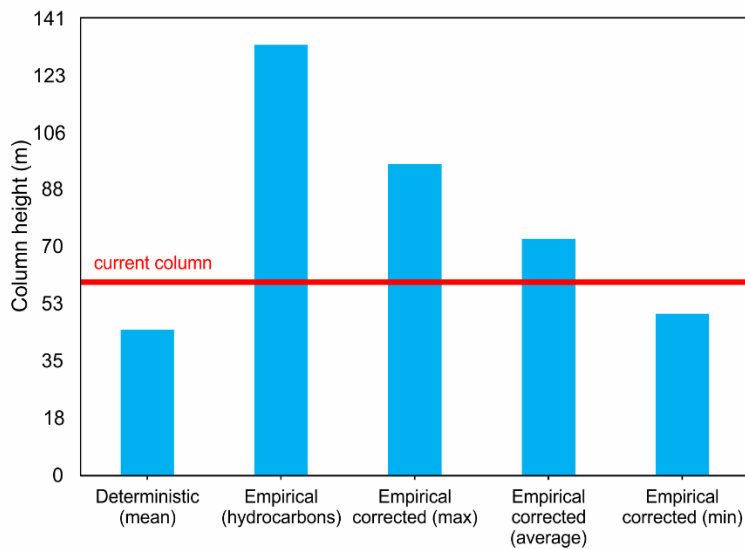
Gas column heights (m)

a) Penola Trough, Katnook gas field (methane)



777

b) Port Campbell, Boggy Creek gas field (CO₂)



778

779

780

781

782

Figure 12. Gas column heights a) Penola Trough, Katnook field b) Port Campbell, Boggy Creek field. Current live columns marked in red. Models shown: deterministic (Sperrevik et al., 2002), empirical (Yielding et al., 2010), empirical corrected max, average and min values (this work).

783

784

7 Conclusions

785

786

787

788

789

790

Two gas fields sealed by fault rocks were examined to compare the standard fault seal analysis techniques applied to methane-brine and CO₂-brine systems. In both cases, the column heights supported by the fault rocks were known, and geochemical gas analysis provided evidence for across-fault connectivity. This allowed us to assess and compare the strengths and weaknesses of two fault seal calibration methods (Sperrevik et al., 2002; Yielding et al., 2010).

791

792

793

794

795

796

The deterministic method predicted critical buoyancy pressure in Katnook (methane) and Boggy Creek (CO₂) fields. The empirical method predicted critical buoyancy pressure in Katnook field and well below threshold pressure in the Boggy Creek field. However, after accounting for uncertainty and applying the newly proposed correction for CO₂, the method also predicted criticality. Thus, the geochemistry and fault seal analysis results corroborate each other.

797

798

799

800

801

802

803

804

805

806

807

808

CO₂ fluid properties and their differences from hydrocarbons have been previously identified as the biggest uncertainty associated with fault seal application to CO₂ systems. However, an extensive literature review showed that a similar spread in IFT values exists within the hydrocarbons, due to the wide range of possible chemical compositions of crude oil. This means that IFT in CO₂-brine system is easier to identify for particular pressure and temperature conditions than in liquid hydrocarbons. Wettability of hydrocarbons is not very well characterised either, and the recent academic focus to CO₂ sequestration applications means that currently far more laboratory experimental data exists for CO₂-brine systems. Perhaps surprisingly, the main challenge in adapting fault seal modelling techniques from hydrocarbons to CO₂ is the uncertainty associated to the hydrocarbon properties.

809

810

811

812

813

814

The two fault seal prediction methods discussed here come with different inherent uncertainties and are best used in conjunction, bearing in mind the differences in the approach. The deterministic method (Sperrevik et al., 2002) can be applied to different fluids via the input of IFT and CA. This work has presented a similar conversion factor system applied to the empirical method (Bretan et al., 2003; Yielding et al., 2010). To do this, an average range of IFT and CA in hydrocarbons

815 under reservoir conditions was determined from literature review. The uncertainty
816 related to the spread in fluid properties was calculated to be 24% of the calculated
817 threshold capillary pressure value. This finding does not change the application of
818 the empirical method, which by definition provides a maximum estimate for capillary
819 threshold pressures. However, it allows to constrain an average and minimum
820 capillary pressure values, which can be used to ascertain 'most likely' and minimum
821 column heights in hydrocarbon exploration. The newly defined average capillary
822 threshold pressure value also allows for better comparison with the deterministic
823 method, which by definition models average rather than maximum pressures.

824 The definition of average IFT and CA of the dataset in the empirical method
825 also allows the conversion of the threshold capillary pressures to other fluid systems,
826 which is desirable for the application to CO₂ sequestration. In application to CO₂
827 storage, where a full column is fully or partially sealed by a fault, the buoyancy
828 pressure must not exceed the minimum threshold capillary pressure value. However,
829 the minimum values discussed here do not equate to safe or recommended
830 buoyancy pressures for CCS contexts. Future studies should define the
831 recommended limit in relation to the minimum threshold capillary pressure values
832 defined here, based on risk analysis and regulatory guidelines.

833

834 8 Acknowledgments

835 This work was supported by an EPSRC PhD studentship in partnership with
836 CO2CRC and Badley Geoscience Ltd. Badley Geoscience are also thanked for the
837 use of the TrapTester software. We thank Peter Boulton and Paul Lyon for providing
838 3D models of Penola Trough and Jennifer Ziesch for sharing the 3D model of Port
839 Campbell and CO2CRC for providing the seismic data. Thanks to Eric Tenthorey for
840 guidance and help with accessing the data. Gareth Johnson was supported by
841 EPSRC Grant EP/P026214/1 and the Faculty of Engineering at the University of
842 Strathclyde.

9 References

- 844 Alipour Tabrizy, V., Denoyel, R., Hamouda, A.A., 2011. Characterization of
845 wettability alteration of calcite, quartz and kaolinite: Surface energy analysis.
846 Colloids Surfaces A Physicochem. Eng. Asp. 384, 98–108.
847 <https://doi.org/10.1016/j.colsurfa.2011.03.021>
- 848 Allan, U.S., 1989. Model for hydrocarbon migration and entrapment within
849 faulted structures. Am. Assoc. Pet. Geol. Bull. 73, 803–811.
- 850 Andrew, M., Bijeljic, B., Blunt, M.J., 2014. Pore-scale contact angle
851 measurements at reservoir conditions using X-ray microtomography. Adv. Water
852 Resour. 68, 24–31. <https://doi.org/10.1016/J.ADVWATRES.2014.02.014>
- 853 Asquith, G.B., Krygowski, D., Gibson, C.R., 2004. Basic well log analysis.
854 American Association of Petroleum Geologists Tulsa.
- 855 Bachu, S., Bennion, D.B., 2009. Interfacial tension between CO₂, freshwater,
856 and brine in the range of pressure from (2 to 27) MPa, temperature from (20 to
857 125) °C, and water salinity from (0 to 334 000) mg L⁻¹. J. Chem. Eng. Data 54, 765–
858 775. <https://doi.org/10.1021/je800529x>
- 859 Barclay, S.A., Worden, R.H., 2009. Effects of reservoir wettability on quartz
860 cementation in oil fields. Quartz Cem. sandstones (Eds RH Worden S. Morad). Spec.
861 Publication 29, 103–117.
- 862 Bense, V.F., Shipton, Z.K., Kremer, Y., Kampman, N., 2016. Fault zone
863 hydrogeology: introduction to the special issue. Geofluids 16, 655–657.
864 <https://doi.org/10.1111/gfl.12205>
- 865 Berg, R.R., 1975. Capillary Pressures in Stratigraphic Traps’.
- 866 Bikkina, P.K., 2011. Contact angle measurements of CO₂–water–
867 quartz/calcite systems in the perspective of carbon sequestration. Int. J. Greenh.
868 Gas Control 5, 1259–1271. <https://doi.org/10.1016/J.IJGGC.2011.07.001>
- 869 Boreham, C.J., Hope, J.M., Jackson, P., Davenport, R., Earl, K.L., Edwards,
870 D.S., Logan, G.A., Krassay, A.A., 2004. Gas – oil – source correlations in the Otway

871 Basin, southern Australia. Petroleum Exploration Society of Australia (PESA), pp.
872 19–22.

873 Boulton, P., Lyon, P., Camac, B., Hunt, S., Zwingmann, H., 2008. Unravelling
874 the complex structural history of the Penola Trough – revealing the St George Fault.
875 PESA East. Australas. Basins Symp. III 14–17.

876 Boulton, P.J., Hibbert, J.E., 2002. The petroleum geology of South Australia.
877 Vol. 1: Otway Basin. 2nd edn. South Australia. Department of Primary Industries
878 and Resources. Petroleum Geology of South Australia Series, Vol. 1.

879 Boulton, P.J., Johns, D.R., Lang, S.C., 2004. Subsurface plumbing of the
880 Crayfish Group in the Penola Trough: Otway Basin, in: Eastern Australasian Basins
881 Symposium II. Petroleum Exploration Society of Australia (PESA), pp. 483–498.

882 Bretan, P., Yielding, G., Jones, H., 2003. Using calibrated shale gouge ratio
883 to estimate hydrocarbon column heights. *Am. Assoc. Pet. Geol. Bull.* 87, 397–413.
884 <https://doi.org/10.1306/08010201128>

885 Bretan, P., Yielding, G., Mathiassen, O.M., Thorsnes, T., 2011. Fault-seal
886 analysis for CO₂ storage: an example from the Troll area, Norwegian Continental
887 Shelf. *Pet. Geosci.* 17, 181–192. <https://doi.org/10.1144/1354-079310-025>

888 Briguglio, D., Hall, M., Keetley, J., 2015. Structural evolution of the Early
889 Cretaceous depocentres, Otway Basin, Victoria. *Aust. J. Earth Sci.* 1–17.
890 <https://doi.org/10.1080/08120099.2015.1084048>

891 Buckley, J.S., Liu, Y., Xie, X., Morrow, N.R., 1997. Asphaltenes and crude oil
892 wetting-the effect of oil composition. *SPE J.* 2, 107–119.

893 Chalbaud, C., Robin, M., Lombard, J.-M., Martin, F., Egermann, P., Bertin,
894 H., 2009. Interfacial tension measurements and wettability evaluation for geological
895 CO₂ storage. *Adv. Water Resour.* 32, 98–109.
896 <https://doi.org/10.1016/J.ADVWATRES.2008.10.012>

897 Chiquet, P., Daridon, J.-L., Broseta, D., Thibeau, S., 2007a. CO₂/water
898 interfacial tensions under pressure and temperature conditions of CO₂ geological

899 storage. *Energy Convers. Manag.* 48, 736–744.
900 <https://doi.org/10.1016/j.enconman.2006.09.011>

901 Chiquet, P., Daridon, J.L., Broseta, D., Thibeau, S., 2007b. CO₂/water
902 interfacial tensions under pressure and temperature conditions of CO₂ geological
903 storage. *Energy Convers. Manag.* 48, 736–744.
904 <https://doi.org/10.1016/j.enconman.2006.09.011>

905 Chivas, A.R., Barnes, I., Evans, W.C., Lupton, J.E., Stone, J.O., 1987. Liquid
906 carbon dioxide of magmatic origin and its role in volcanic eruptions. *Nature* 326,
907 587–589. <https://doi.org/10.1038/326587a0>

908 Cockshell, C.D., O'Brien, G.W., McGee, A., Lovibond, R., Perincek, D.,
909 Higgins, R., 1995. Western Otway Crayfish Group troughs. *APPEA J.* 35, 385–404.

910 Dance, T., 2013. Assessment and geological characterisation of the
911 CO₂CRC Otway Project CO₂ storage demonstration site: From prefeasibility to
912 injection. *Mar. Pet. Geol.* 46, 251–269.
913 <https://doi.org/10.1016/j.marpetgeo.2013.06.008>

914 Danesh, A., 1998. PVT and phase behaviour of petroleum reservoir fluids.
915 Elsevier.

916 Daniel, R.F., Kaldi, J.G., 2009. Evaluating Seal Capacity of Cap Rocks and
917 Intraformational Barriers for CO₂ Containment 335–345.
918 <https://doi.org/10.1306/13171247St59227>

919 Duddy, I.R., 1997. Focussing exploration in the Otway Basin: understanding
920 timing of source rock maturation. *APPEA J.* 37, 178–191.

921 Espinoza, D.N., Santamarina, J.C., 2010. Water-CO₂ -mineral systems:
922 Interfacial tension, contact angle, and diffusion-Implications to CO₂ geological
923 storage. *Water Resour. Res.* 46. <https://doi.org/10.1029/2009WR008634>

924 Jennings, H.Y., Newman, G.H., 1971. The effect of temperature and
925 pressure on the interfacial tension of water against methane-normal decane
926 mixtures. *Soc. Pet. Eng. J.* 11, 171–175.

927 Farokhpoor, R., Bjørkvik, B.J.A., Lindeberg, E., Torsæter, O., 2013. CO2
928 Wettability Behavior During CO2 Sequestration in Saline Aquifer -An Experimental
929 Study on Minerals Representing Sandstone and Carbonate. *Energy Procedia* 37,
930 5339–5351. <https://doi.org/10.1016/J.EGYPRO.2013.06.452>

931 Faulkner, D.R., Jackson, C.A.L., Lunn, R.J., Schlische, R.W., Shipton, Z.K.,
932 Wibberley, C.A.J., Withjack, M.O., 2010. A review of recent developments
933 concerning the structure, mechanics and fluid flow properties of fault zones. *J. Struct.*
934 *Geol.* 32, 1557–1575.

935 Firoozabadi, A., Ramey, H.J., Ramey Jr, H.J., 1988. Surface tension of
936 water-hydrocarbon systems at reservoir conditions. *J. Can. Pet. Technol.* 27.

937 Fisher, Q.J., Knipe, R.J., 1998. Fault sealing processes in siliciclastic
938 sediments. *Geol. Soc. London, Spec. Publ.* 147, 117–134.
939 <https://doi.org/10.1144/GSL.SP.1998.147.01.08>

940 Flock, D.L., Le, T.H., Gibeau, J.P., 1986. The effect of temperature on the
941 interfacial tension of heavy crude oils using the pendent drop apparatus. *J. Can. Pet.*
942 *Technol.* 3.

943 Georgiadis, A., Maitland, G., Trusler, J.P.M., Bismarck, A., 2010. Interfacial
944 tension measurements of the (H2O + CO2) system at elevated pressures and
945 temperatures. *J. Chem. Eng. Data* 55, 4168–4175.
946 <https://doi.org/10.1021/je100198g>

947 Ghorbani, M., Mohammadi, A.H., 2017. Effects of temperature, pressure and
948 fluid composition on hydrocarbon gas - oil interfacial tension (IFT): An experimental
949 study using ADSA image analysis of pendant drop test method. *J. Mol. Liq.* 227,
950 318–323. <https://doi.org/10.1016/J.MOLLIQ.2016.11.110>

951 Gibson, R.G., 1998. Physical character and fluid-flow properties of
952 sandstone-derived fault zones. *Geol. Soc. London, Spec. Publ.* 127, 83–97.

953 Gluyas, J.G., Hitchens, H.M., 2003. United Kingdom oil and gas fields:
954 commemorative millennium volume.

955 Guariguata-Rojas, G.J., Underhill, J.R., 2017. Heriot-Watt University
956 Implications of Early Cenozoic uplift and fault reactivation for carbon storage in the
957 Moray Firth Basin Implications of Early Cenozoic uplift and fault reactivation for
958 carbon storage in the Moray Firth Basin. <https://doi.org/10.1190/int-2017-0009.1>

959 Hassan, M.E., Nielsen, R.F., Calhoun, J.C., 1953. Effect of Pressure and
960 Temperature on Oil-Water Interfacial Tensions for a Series of Hydrocarbons. *J. Pet.*
961 *Technol.* 5, 299–306. <https://doi.org/10.2118/298-G>

962 Higgs, K.E., Haese, R.R., Golding, S.D., Schacht, U., Watson, M.N., 2015.
963 The Pretty Hill Formation as a natural analogue for CO₂ storage: An investigation of
964 mineralogical and isotopic changes associated with sandstones exposed to low,
965 intermediate and high CO₂ concentrations over geological time. *Chem. Geol.* 399,
966 36–64. <https://doi.org/10.1016/j.chemgeo.2014.10.019>

967 Hjelmeland, O.S., Larrondo, L.E., 1986. Experimental Investigation of the
968 Effects of Temperature, Pressure, and Crude Oil Composition on Interfacial
969 Properties. *SPE Reserv. Eng.* 1, 321–328. <https://doi.org/10.2118/12124-PA>

970 Hough, E.W., Rzasa, M.J., Wood, B.B., Oil, S., Co, G., 1951. Interfacial
971 Tensions at Reservoir Pressures and Temperatures ; Apparatus and the Water-
972 Methane System. *J. Pet. Trans. AIME* 192, 57–60. <https://doi.org/10.2118/951057-G>

973 Iglauer, S., 2018. Optimum storage depths for structural CO₂ trapping. *Int. J.*
974 *Greenh. Gas Control* 77, 82–87. <https://doi.org/10.1016/J.IJGGC.2018.07.009>

975 Iglauer, S., Pentland, C.H., Busch, A., 2015. CO₂ wettability of seal and
976 reservoir rocks and the implications for carbon geo-sequestration. *Water Resour.*
977 *Res.* 51, 729–774. <https://doi.org/10.1002/2014WR015553>

978 Jung, J.-W., Wan, J., 2012. Supercritical CO₂ and Ionic Strength Effects on
979 Wettability of Silica Surfaces: Equilibrium Contact Angle Measurements. *Energy &*
980 *Fuels* 26, 6053–6059. <https://doi.org/10.1021/ef300913t>

981 Kalantari Meybodi, M., Daryasafar, A., Karimi, M., 2016. Determination of
982 hydrocarbon-water interfacial tension using a new empirical correlation. *Fluid Phase*
983 *Equilib.* 415, 42–50. <https://doi.org/10.1016/J.FLUID.2016.01.037>

- 984 Karolyt , R., 2018. The migration and retention of CO₂ and methane in the
985 Otway Basin and south-east Australia: an integrated geochemical and structural
986 analysis. University of Edinburgh.
- 987 Karolyt , R., Johnson, G., Gy re, D., Serno, S., Flude, S., Stuart, F.M.,
988 Chivas, A.R., Boyce, A., Gilfillan, S.M.V., 2019. Tracing the migration of mantle CO₂
989 in gas fields and mineral water springs in south-east Australia using noble gas and
990 stable isotopes. *Geochim. Cosmochim. Acta* 259, 109–128.
- 991 Kashafi, K., 2012. Measurement and modelling of interfacial tension and
992 viscosity of reservoir fluids. Thesis. Heriot-Watt University.
- 993 Knipe, R.J., 1997. Juxtaposition and seal diagrams to help analyze fault
994 seals in hydrocarbon reservoirs. *Am. Assoc. Pet. Geol. Bull.* 81, 187–195.
- 995 Lehner, F.K., Pilaar, W.F., 1997. The emplacement of clay smears in
996 synsedimentary normal faults: inferences from field observations near Frechen,
997 Germany, in: *Norwegian Petroleum Society Special Publications*. Elsevier, pp. 39–
998 50.
- 999 Lindsay, N.G., Murphy, F.C., Walsh, J.J., Watterson, J., Flint, S., Bryant, I.D.,
1000 1993. Outcrop studies of shale smears on fault surfaces. *Geol. Model. Hydrocarb.*
1001 *Reserv. outcrop Analog.* 15, 113–123.
- 1002 Lisk, M., 2004. Constraints on the oil prospectivity of the Penola Trough,
1003 onshore Otway Basin.
- 1004 Little, B.M., Phillips, S.E., 1995. Detrital and authigenic mineralogy of the
1005 Pretty Hill Formation in the Penola Trough, Otway Basin: implications for future
1006 exploration and production. *APPEA J.* 35, 538–557.
- 1007 Liu, Y., Li, H.A., Okuno, R., 2016. Measurements and Modeling of Interfacial
1008 Tension for CO₂/CH₄/Brine Systems under Reservoir Conditions. *Ind. Eng. Chem.*
1009 *Res.* 55, 12358–12375. <https://doi.org/10.1021/acs.iecr.6b02446>
- 1010 Lovibond, R., Suttill, R.J., Skinner, J.E., Aburas, A.N., 1995. The
1011 hydrocarbon potential of the Penola Trough, Otway Basin. *APPEA J.* 35, 358–371.

- 1012 Lyon, Boulton, P.J., Hillis, R.R., Mildren, S.D., 2005. Sealing by Shale Gouge
1013 and Subsequent Seal Breach by Reactivation: A Case Study of the Zema Prospect,
1014 Otway Basin. Eval. fault cap rock seals AAPG Hedb. Ser. no. 2 179–197.
1015 <https://doi.org/10.1306/1060764H23169>
- 1016 Lyon, P.J., Boulton, P.J., Hillis, R.R., Bierbrauer, K., 2007. Basement controls
1017 on fault development in the Penola Trough, Otway Basin, and implications for fault-
1018 bounded hydrocarbon traps. Aust. J. Earth Sci. 54, 675–689.
1019 <https://doi.org/10.1080/08120090701305228>
- 1020 Lyon, P.J., Boulton, P.J., Mitchell, a, Hillis, R.R., 2004. Improving fault
1021 geometry interpretation through ‘ pseudo-depth ’ conversion of seismic data in the
1022 Penola Trough , Otway Basin . 19–22.
- 1023 Lyon, P.J., Boulton, P.J., Watson, M.N., Hillis, R., 2005. A systematic fault seal
1024 evaluation of the Ladbroke Grove and Pyrus traps of the Penold Trough, Otway
1025 Basin. Aust. Pet. Prod. Explor. Assoc. J. 45, 459–476.
- 1026 Miocic, J.M., Gilfillan, S.M.V., Roberts, J.J., Edlmann, K., McDermott, C.I.,
1027 Haszeldine, R.S., 2016. Controls on CO₂ storage security in natural reservoirs and
1028 implications for CO₂ storage site selection. Int. J. Greenh. Gas Control 51, 118–125.
1029 <https://doi.org/10.1016/j.ijggc.2016.05.019>
- 1030 Miocic, J.M., Johnson, G., Bond, C.E., 2019. Uncertainty in fault seal
1031 parameters: implications for CO₂ column height retention and storage capacity in
1032 geological CO₂ storage projects. Solid Earth 10, 951–967.
1033 <https://doi.org/10.5194/se-10-951-2019>
- 1034 Najafi-Marghmaleki, A., Tatar, A., Barati-Harooni, A., Mohebbi, A., Kalantari-
1035 Meybodi, M., Mohammadi, A.H., 2016. On the prediction of interfacial tension (IFT)
1036 for water-hydrocarbon gas system. J. Mol. Liq. 224, 976–990.
1037 <https://doi.org/10.1016/J.MOLLIQ.2016.10.083>
- 1038 Naylor, M., Wilkinson, M., Haszeldine, R.S., 2010. Calculation of CO₂
1039 column heights in depleted gas fields from known pre-production gas column
1040 heights. Mar. Pet. Geol. <https://doi.org/10.1016/j.marpetgeo.2010.10.005>

1041 Nordgard Bolas, H.M., Hermanrud, C., Teige, G.M.G., 2005. Seal capacity
1042 estimation from subsurface pore pressures. *Basin Res.* 17, 583–599.
1043 <https://doi.org/10.1111/j.1365-2117.2005.00281.x>

1044 Øren, P.-E., Bakke, S., 2003. Reconstruction of Berea sandstone and pore-
1045 scale modelling of wettability effects. *J. Pet. Sci. Eng.* 39, 177–199.
1046 [https://doi.org/10.1016/S0920-4105\(03\)00062-7](https://doi.org/10.1016/S0920-4105(03)00062-7)

1047 Pei, Y., Paton, D.A., Knipe, R.J., Wu, K., 2015. A review of fault sealing
1048 behaviour and its evaluation in siliciclastic rocks. *Earth-Science Rev.* 150, 121–138.
1049 <https://doi.org/10.1016/j.earscirev.2015.07.011>

1050 Peng, D.-Y., Robinson, D.B., 1976. A new two-constant equation of state.
1051 *Ind. Eng. Chem. Fundam.* 15, 59–64.

1052 Radke, C.J., Kavscek, A.R., Wong, H., 1992. A Pore-Level Scenario for the
1053 Development of Mixed Wettability in Oil Reservoirs, in: *SPE Annual Technical*
1054 *Conference and Exhibition*. Society of Petroleum Engineers.
1055 <https://doi.org/10.2118/24880-MS>

1056 Rajayi, M., Kantzas, A., 2011. Effect of Temperature and Pressure on
1057 Contact Angle and Interfacial Tension of Quartz/Water/Bitumen Systems. *J. Can.*
1058 *Pet. Technol.* 50, 61–67. <https://doi.org/10.2118/148631-PA>

1059 Ren, Q.Y., Chen, G.J., Yan, W., Guo, T.M., 2000. Interfacial tension of (CO₂
1060 + CH₄) + water from 298 K to 373 K and pressures up to 30 MPa. *J. Chem. Eng.*
1061 *Data* 45, 610–612. <https://doi.org/10.1021/jc990301s>

1062 Rimstidt, J.D., Barnes, H.L., 1980. The kinetics of silica-water reactions.
1063 *Geochim. Cosmochim. Acta* 44, 1683–1699. [https://doi.org/10.1016/0016-](https://doi.org/10.1016/0016-7037(80)90220-3)
1064 [7037\(80\)90220-3](https://doi.org/10.1016/0016-7037(80)90220-3)

1065 Robert M. Sneider, J.S.S.G.W.B., Neasham, J.W., 1997. *AAPG Memoir 67:*
1066 *Seals, Traps, and the Petroleum System*. Chapter 1: Comparison of Seal Capacity
1067 Determinations: Conventional Cores vs. Cuttings 1–12.

1068 Schowalter, T.T., 1974. *AAPG bulletin., AAPG Bulletin*. American
1069 Association of Petroleum Geologists.

1070 Shipton, Z.K., Cowie, P.A., 2001. Damage zone and slip-surface evolution
1071 over μm to km scales in high-porosity Navajo sandstone, Utah. *J. Struct. Geol.* 23,
1072 1825–1844. [https://doi.org/10.1016/S0191-8141\(01\)00035-9](https://doi.org/10.1016/S0191-8141(01)00035-9)

1073 Shipton, Z.K., Evans, J.P., Robeson, K.R., Forster, C.B., Snelgrove, S., 2002.
1074 Structural heterogeneity and permeability in faulted eolian sandstone: Implications
1075 for subsurface modeling of faults. *AAPG Bull.* v 86, 863–883.

1076 Singh, K., Bijeljic, B., Blunt, M.J., 2016. Imaging of oil layers, curvature and
1077 contact angle in a mixed-wet and a water-wet carbonate rock. *Water Resour. Res.*
1078 52, 1716–1728. <https://doi.org/10.1002/2015WR018072>

1079 Sperrevik, S., Gillespie, P.A., Fisher, Q.J., Halvorsen, T., Knipe, R.J., 2002.
1080 Empirical estimation of fault rock properties. *Nor. Pet. Soc. Spec. Publ.* 11, 109–125.
1081 [https://doi.org/10.1016/S0928-8937\(02\)80010-8](https://doi.org/10.1016/S0928-8937(02)80010-8)

1082 Sutjiadi-Sia, Y., Jaeger, P., Eggers, R., 2008. Interfacial phenomena of
1083 aqueous systems in dense carbon dioxide. *J. Supercrit. Fluids* 46, 272–279.
1084 <https://doi.org/10.1016/J.SUPFLU.2008.06.001>

1085 Sutton, R.P., 2006. Oil system correlations. *LAKE, LW Pet. Eng. Handbook.*
1086 *Soc. Pet. Eng.* 1, 258–306.

1087 Tassone, D.R., Holford, S.P., Duddy, I.R., Green, P.F., Hillis, R.R., 2014.
1088 Quantifying Cretaceous–Cenozoic exhumation in the Otway Basin, southeastern
1089 Australia, using sonic transit time data: Implications for conventional and
1090 unconventional hydrocarbon prospectivity. *Am. Assoc. Pet. Geol. Bull.* 98, 67–117.
1091 <https://doi.org/10.1306/04011312111>

1092 Teasdale, J.P., Pryer, L.L., Stuart-Smith, P.G., Romine, K.K., Etheridge,
1093 M.A., Loutit, T.S., Kyan, D.M., 2003. Structural framework and basin evolution of
1094 Australia’s southern margin. *APPEA J.* 43, 13–37.

1095 Tenthorey, E., Dance, T., Cinar, Y., Ennis-King, J., Strand, J., 2014. Fault
1096 modelling and geomechanical integrity associated with the CO₂CRC Otway 2C
1097 injection experiment. *Int. J. Greenh. Gas Control* 30, 72–85.
1098 <https://doi.org/10.1016/j.ijggc.2014.08.021>

- 1099 Tian Yi-Ling, T., Yan-Fan, X., Hong-Xu, Z., Xi-Jing, D., Xiao-Wen, R., Feng-
1100 Cai, Z., Yi-Ling, T., Yan-Fan, X., Hong-Xu, Z., Xi-Jing, D., Xiao-Wen, R., Feng-Cai,
1101 Z., 1997. Interfacial Tensions between Water and Non-polar Fluids at High
1102 Pressures and High Temperatures. *Acta Physico-Chimica Sin.* 13, 89–95.
1103 <https://doi.org/10.3866/PKU.WHXB19970120>
- 1104 Treiber, L.E., Owens, W.W., 1972. A Laboratory Evaluation of the Wettability
1105 of Fifty Oil-Producing Reservoirs. *Soc. Pet. Eng. J.* 12, 531–540.
1106 <https://doi.org/10.2118/3526-PA>
- 1107 Vavra, C.L., Kaldi, J.G., Sneider, R.M., 1992. Geological applications of
1108 capillary pressure: a review (1). *Am. Assoc. Pet. Geol. Bull.* 76, 840–850.
- 1109 Watson, M.N., Boreham, C.J., Tingate, P.R., 2004. Carbon dioxide and
1110 carbonate cements in the Otway Basin; implications for geological storage of carbon
1111 dioxide. *APPEA J.* 44, 703–720.
- 1112 Watson, M.N., Zwingmann, N., Lemon, N.M., Tingate, P.R., 2003. Onshore
1113 Otway Basin carbon dioxide accumulations: CO₂-induced diagenesis in natural
1114 analogues for underground storage of greenhouse gas. *APPEA J.* 43, 637–653.
- 1115 Watts, N.L., 1987. Theoretical aspects of cap-rock and fault seals for single-
1116 and two-phase hydrocarbon columns. *Mar. Pet. Geol.* 4, 274–307.
1117 [https://doi.org/10.1016/0264-8172\(87\)90008-0](https://doi.org/10.1016/0264-8172(87)90008-0)
- 1118 Wiegand, G., Franck, E.U., 1994. Interfacial tension between water and non-
1119 polar fluids up to 473 K and 2800 bar. *Berichte der Bunsengesellschaft für Phys.*
1120 *Chemie* 98, 809–817. <https://doi.org/10.1002/bbpc.19940980608>
- 1121 Worden, R.H., Morad, S., 2000. Economic evaluation of a petroleum
1122 accumulation demands a Quartz cementation in oil field sandstones: a review of
1123 the key controversies. *Spec. Publs int. Ass. Sediment* 29, 1–20.
- 1124 Yielding, G., 2002. Shale Gouge Ratio — calibration by geohistory. *Nor. Pet.*
1125 *Soc. Spec. Publ.* 11, 1–15. [https://doi.org/10.1016/S0928-8937\(02\)80003-0](https://doi.org/10.1016/S0928-8937(02)80003-0)

- 1126 Yielding, G., Bretan, P., Freeman, B., 2010. Fault seal calibration: a brief
1127 review. *Geol. Soc. London, Spec. Publ.* 347, 243–255.
1128 <https://doi.org/10.1144/SP347.14>
- 1129 Yielding, G., Freeman, B., Needham, D.T., 1997. Quantitative fault seal
1130 prediction. *Am. Assoc. Pet. Geol. Bull.* 81, 897–917.
- 1131 Ziesch, J., Aruffo, C.M., Tanner, D.C., Beilecke, T., Dance, T., Henk, A.,
1132 Weber, B., Tenthorey, E., Lippmann, A., Krawczyk, C.M., 2017. Geological structure
1133 and kinematics of normal faults in the Otway Basin, Australia, based on quantitative
1134 analysis of 3-D seismic reflection data. *Basin Res.* 29, 129–148.
1135 <https://doi.org/10.1111/bre.12146>
- 1136 Ziesch, J., Aruffo, C.M., Tanner, D.C., Beilecke, T., Dance, T., Henk, A.,
1137 Weber, B., Tenthorey, E., Lippmann, A., Krawczyk, C.M., 2015. Geological structure
1138 and kinematics of normal faults in the Otway Basin, Australia, based on quantitative
1139 analysis of 3-D seismic reflection data. *Basin Res.* n/a-n/a.
1140 <https://doi.org/10.1111/bre.12146>